

Fabrication and Measurement of Graphene Devices

Ian Wilkes

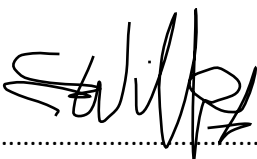
August 2019

This thesis is submitted in partial fulfilment of the requirements
for the degree of Master of Science.

Department of Physics,
Lancaster University, UK.

Declaration

This thesis results entirely from my own work and has not been offered previously for any other degree or diploma.

Signature

ABSTRACT

Graphene, an allotrope of carbon, has been prepared by mechanical exfoliation and Chemical Vapour Deposition. The graphene so produced has been micro manipulated using polymer membranes and optical microscopy and so placed on silicon wafer. In addition, individual graphene fragments were micro manipulated and placed on pre-prepared hexagonal boron nitride flakes to aid in the fabrication of devices for testing. Graphene devices were prepared by sequential lithography, metalisation and plasma treatment to make field effect multi terminal Hall bar test pieces. The Hall bar geometry test pieces were examined at a variety of magnetic field strengths between 11 Tesla and zero magnetic field. By careful control of the gate voltage, temperature the I-V characteristics of the Hall bar test pieces were measured. Analysis of the I-V characteristics as a function of gate voltage and magnetic field strength was undertaken to determine the location of Dirac cones. Simple analysis of resistance change with gate voltage and magnetic field strength resulted in identification of the first parts of the Hofstadter energy spectrum. To help fabricate multilayer mesas of graphene and hexagonal boron nitride a micromanipulator workstation and simple UV microscope were constructed.

ACKNOWLEDGEMENTS

I would like to thank my supervisor Dr Leonard Ponomarenko for his invaluable guidance and encouragement. I would especially like to thank the clean room managers and technical staff whom without their efforts many of the activities for device fabrication would have not been possible.

I am also grateful to the Department of Physics at Lancaster University for the opportunity to both learn and teach physics and the continuous support for improvement. I have greatly enjoyed teaching as a PGTA and this has been instrumental in deciding to continue teaching physics at school; many aspects of a physics pedagogical approach I have learnt whilst teaching.

My very special thanks and gratitude goes to my wife Xueling and my understanding children Sebastian and Poppy-Mae for whom their patience and unwavering support throughout this journey has been gratefully received. The interest shown by Sebastian and Poppy-Mae during school holidays is always encouraging and I hope they enjoyed using Lancaster University Library and facilities as much as myself. The educational opportunity of using excellent facilities at a young age I hope will add to their enthusiasm for learning.

CONTENTS

Abstract	3
Acknowledgements	4
Abbreviations	6
List of Figures and Tables	7
Chapter 1. Graphene Introduction	9
1.2 Graphene structure.	12
1.3 Graphene Dispersion Relationship and Electronic structure	14
1.4 Electron Transport Properties of Graphene.	18
1.5 Graphene Superlattice	22
1.6 Conclusion and Summary	28
1.7 References	29
Chapter 2 Raman Spectral Analysis.	31
2.1 Introduction	31
2.2 Raman theory	31
2.3 Graphene Raman Explanation.	35
2.4 Graphene Raman peaks for identification.	38
2.5 Raman Analysis.	38
2.6 Raman Analysis of Presented Spectra	39
2.7 Graphene and Defects.	42
2.8 References	45
Chapter 3: Experimental Preparation of Graphene and Graphene stacks	46
3.1 CVD of Graphene	46
3.2 Recrystallisation of hexagonal boron nitride.	48
3.3 Ultra-Violet Microscopy	48
3.3.1 Manufacture of 2D Graphene Transfer Station	50
3.4 Experimental Transfer Procedure	53
3.5 Lithography to Fabricate Devices.	54
3.6 Multilayer 2D stacking for Super lattices.	61
3.7 References.	62
Chapter 4. Measurement of Electrical and Magnetic properties of Graphene	63
4.1 Connector for Graphene measurement	63
4.2 Device Measurement Analysis	66
4.3 Review of Data Analysis	71
4.4 Conclusion	73
4.5. Next steps	73
4.6 References	73
Appendix	74

ABBREVIATIONS

sccm	Standard Cubic Centimetres per Minute
CVD	Chemical Vapour Deposition
hBN	Hexagonal Boron Nitride
SEM	Scanning Electron microscope

LIST OF FIGURES AND TABLES

Figure 1. Crystals of graphite	10
Figure 2. Shows a colour plot for the expected contrast as a function of wavelength.	10
Figure 3. The formation of sp^2 hybrid orbitals from 2s and 2p electrons.	11
Figure 4. Showing the carbon-carbon bond layout of graphene.	12
Figure 5. The Bravais primitive cell making up the honey-comb lattice b. the first Brillouin zone.	13
Figure 6. Showing the A - B pattern of sub lattices in graphene.	13
Figure 7. Showing band gap, E_g , of a typical semi conductor.	14
Figure 8. Dispersion diagram for graphene, the Energy E_k is given relative to the Dirac point.	15
<i>Figure 9. Shift in Fermi level as doping changes.</i>	16
<i>Figure 10. Showing the spin (σ) and momentum vector k for each sub lattice A and B.</i>	17
<i>Figure 11. Graphene Landau levels and Quantum Hall levels taken from Zhang.</i>	21
<i>Figure 12. (a) The original figure of Hofstadter.</i>	22
<i>Figure 13. Showing Moiré pattern of graphene on h BN with 5° mis-alignment</i>	25
<i>Figure 14. Formation of Multiple Dirac cones with graphene on hexagonal boron nitride</i>	25
<i>Figure 15. Wannier diagram for graphene.</i>	27
<i>Figure 15b. Wannier calculation for a hexagonal lattice</i>	27
Figure 16. Change of polarisability α with graphene crystal moment space	33
Figure 17. Feynman diagram for a simple Raman process	34
Figure 18. Simplified energy diagram for processes occurring in Raman scattering	35
Figure 19. Simplified sketch of the Raman microscope used to analyse graphene fragments.	36
Figure 20. Graphite, multi layer graphene and graphene Raman spectrum overlaid	38
Figure 21. The two vibrations leading to changes in polarisability in a 2D crystal of graphene	39
Figure 22. The main Raman active peaks for graphene, G, D, D' and 2D	39
Figure 23. Raman spectrum of highly defect concentration graphene	40
Figure 24. Raman spectrum of CVD graphene taken at 514 nm	40

Table1. Data of Raman Spectroscopy data for flake testing	39
Figure 25. High quality "single layer" graphene from mechanical exfoliation.	40
Figure 26. Thick graphene (many layers) or thin graphite to compare signal response	41
Figure 27. Raman spectrum of Bilayer graphene	41
Figure 28. Graphene from methane over copper and removed with ferric chloride	42
Figure 29. Raman spectrum of graphene irradiated by electron beam.	49
Figure 30. UV-visible-IR spectrum of a graphene solution.	55
Figure 31. Light path for UV modified microscope	56
Table 2. Transfer station microscope configuration.	51
Figure 32. Difference between infinity and 160 (finite) tube objective lens systems.	58
Figure 33. Photograph of stacking "transfer station" with photograph inset of x,y,z control	59
Figure 34. Schematic of AutoCAD alignment and pad Ebeam lithography	63
Figure 35. Dye exposure results in photochemical reaction, the	67
Figure 36a. Leadless Chip Carrier (LCC), Figure 36 b. Head of (variable temperature) probe.	74
Figure 37. Schematic diagram of structure of cryostat for I-V measurement of graphene.	75
Figure 38. Set up for measurement of Hall voltage measurement (V_{Hall}) with magnetic field.	78
Figure 39. Measurement showing control of gate voltage (V_{gate}) for Hall Bar.	79
Figure 40. Plot of Resistance (Ohm) on a surface graph of Gate Voltage (V_{gate}) and Magnetic field (B_z)	81
Figure 41. Plot of resistance at zero gate voltage (V_o) versus magnetic field strength. Data from figure 40 (b).	82
Figure 42. Plot of R_{max} only taken from data shown in figure 40.	84
Figure 43. Plot of gradients of families of connected points from Figure 41	85
Figure 44. Plot of n/n_o versus an inverse of magnetic field (B_z /Tesla).	86
Table 3. Values of δB_z (Tesla) of maximum resistance (at n/n_o)	86
Figure 45. R_{max} of points not associated with series from figure 43	87

1.1 GRAPHENE INTRODUCTION

Graphene was defined in 1994 as “the individual carbon layers in graphite intercalation compounds.”¹ However, note that this definition relied on the carbon network to be part of a larger structure; the graphene did not exist in isolation. The crystallographic structure of graphite² is composed of layers of hexagonally-arranged carbon atoms, stacked in a AB formation with the individual layers of carbon separated by 0.342 nm in the z-direction. The crystallographic z-spacing is much larger than that of the carbon-carbon spacing within the same layer, which is 0.142 nm. Graphene had been studied theoretically by Wallace³ in 1947 as a single layer of graphite,⁴ as a way to model graphite. Experimentally, the only evidence of thin graphitic layers was found on the surface of SiC after the substrate was heated in vacuum,⁵ the paper was not definitive in the characterization of the graphene. The isolation of individual 2D crystal species was widely believed to be thermodynamically unstable and therefore impossible to isolate by experiment.^{6,7} This idea was disproved in 2004 when researchers at the University of Manchester became the first to successfully isolate monolayers of graphene through a mechanical exfoliation method using a pure graphite sample and (scotch) tape.⁸ Figure 1 demonstrates that the graphene was able to be observed on a silicon-silicondioxide wafer, the interference contrast enabled the monolayer graphene to be observed.⁹ The thickness of the silicondioxide layer is important for observing the graphene layers; silicon is reflective to visible light, silicon dioxide is transparent; hence the silicondioxide layers can act as an interference filter. As the eye is most sensitive to green light of wavelength 555nm¹⁰ the silicondioxide layer can be chosen so that maximum contrast is at this wavelength. Figure 2 shows the variation of wavelength of light with silicondioxide thickness to produce a variation in contrast. In this work a silicondioxide layer thickness of 290 nm was chosen.

Adhesive tape was used to remove individual layers from highly-oriented pyrolytic graphite (HOPG) and the resulting material was transferred to a silicon/silicondioxide substrate as Figure 1. Monolayer and few-layer graphene were identified through a combination of optical and atomic force microscope (AFM) imaging. A selected few-layer graphene was patterned into a Hall bar structure to study the electronic properties of the material, and a metallic field-effect transistor was implemented. Less than a year after their initial discovery, Geim and Novoselov successfully performed the first electronic transport measurements on monolayer graphene.¹¹ Bulk graphite is made up of a periodic arrangement of individual graphene layers held together by Van-der-Waals forces, with an interlayer spacing of 0.34

nm. Individual graphene monolayers are composed of a hexagonal array of carbon atoms spaced 0.142 nm(1.42 Å) apart. The isolated carbon atom has an electron structure described as such:

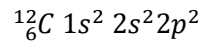


Figure 1. Crystals of graphite on LHS are separated using pressure sensitive tape to form layers of graphene (RHS); the layers of graphene can be observed using white light.

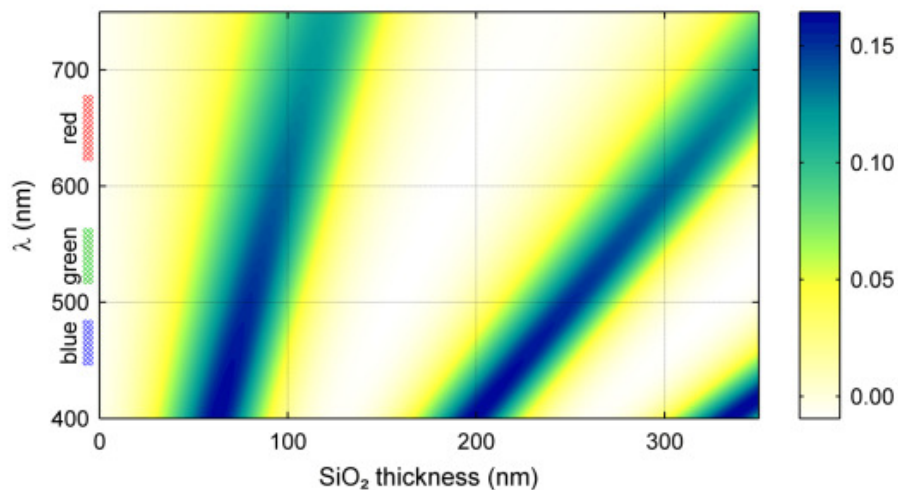


Figure 2. Shows a colour plot for the expected contrast as a function of wavelength and silicon-dioxide (SiO_2) thickness as a function of incident white light. Taken from Blake et al.¹² In this work at Lancaster, 290nm silicon dioxide coated silicon wafers are used.

The $1s^2$ electrons are (far) lower in potential energy than the four $2s^2 2p^2$ electrons and will be ignored in this analysis. In the graphene allotrope of carbon, the three nearest neighbours are arranged

symmetrically around a carbon atom. The mixing of $2s^2 2p^1$ electrons in $(2)sp^2$ hybridised energy levels as shown in 3. The $(2)sp^2$ gives the triangular pattern around each carbon atom with an angle of 120° between each carbon-carbon bond. The three electrons give a strongly bonded planar structure, and these $(2)sp^2$ structures lead to the graphene the honeycomb lattice. The remaining $2p_z^1$ electron is responsible for the electrical properties and this aspect will be dealt with at greater length in the next section.

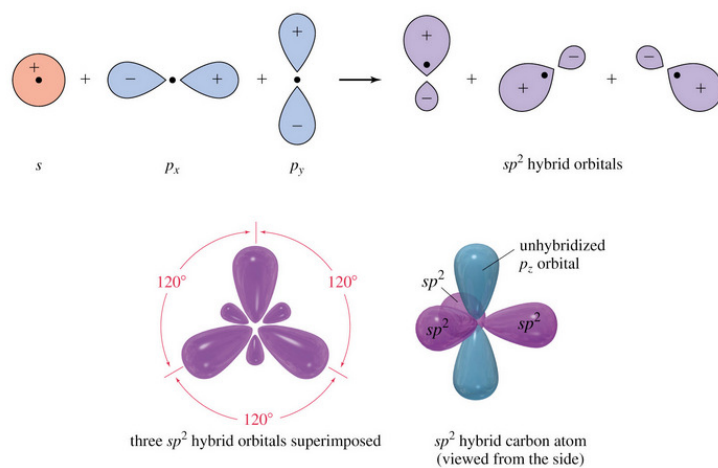


Figure 3. The formation of sp^2 hybrid orbitals from $2s$ and $2p$ electrons. Three sp^2 orbitals form a planar structure. The remaining unhybridised p_z orbital is symmetric about the plane formed by the sp^2 orbitals.

The many electronic properties of graphene are best described by the $2p_z^1$ electron per carbon atom, ie $2p_z^1$ per carbon atom in the graphene structure. That is, in the primitive unit cell there are two carbon atoms (A and B) each contributing exactly one electron (vide infra). The mechanical properties of the monolayer is a result of the strong C-C σ -bond (Figure 4).

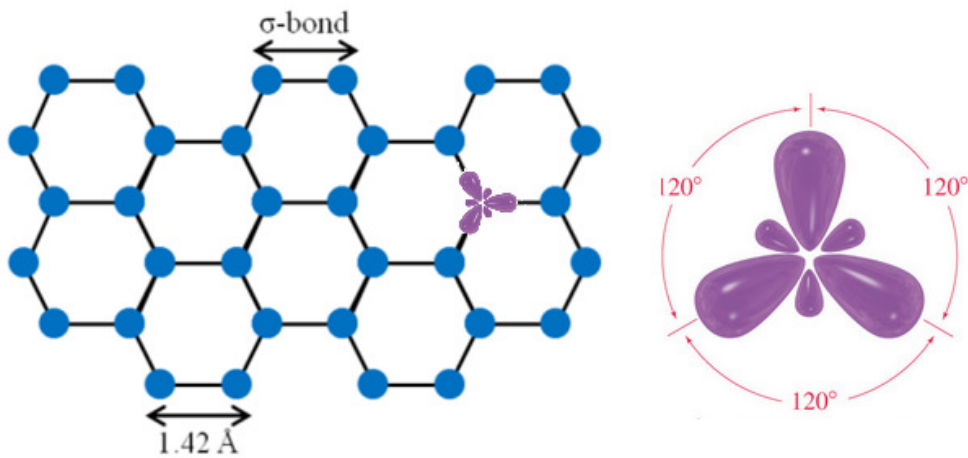


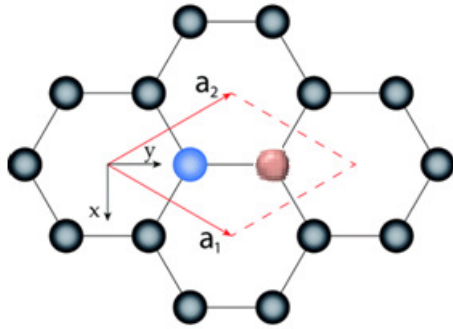
Figure 4. Showing the carbon-carbon bond layout of graphene, of length 0.142 nm, the blue dots representing the carbon atom nuclear centers. The sp^2 orbitals are shown in purple and the relative arrangement in the honeycomb lattice making up the sigma (σ) bonds of graphene.

These sigma bonds allow graphene to exhibit a high level of mechanical strength, even though the material is atomically thin. To break any carbon-carbon bond requires 4.84×10^{-20} J (per bond).¹³ The fourth electron is perpendicular to the sigma bond layer in the molecular p-orbital and participates in electronic conduction.¹⁴

1.2 GRAPHENE STRUCTURE.

As the experiments by Geim and Novoselov demonstrated in 2004, the resultant graphene monolayer has exactly the same atomic layout as the layers in graphite. The carbon-carbon bond lengths in graphene are 0.142 nm, exactly the same as graphite, the symmetry, $p6mm$, the same symmetry as the layers found in graphite. Figure 5 a, b shows the crystal structure and reciprocal lattice of graphene respectively. The Bravais primitive cell in Figure 6 clearly shows that there are two carbon atoms per unit cell. In order to separate a graphene layer from the graphite an amount of energy needs to be supplied. The energy is applied to the graphite surface via the use of a pressure sensitive tape (commonly called cellotape). Studies of graphite-graphene interaction suggest the energy of interaction per atom of 61 meV,¹⁵ giving an approximate cleavage energy per square mm of 1nJ.

a.



b.

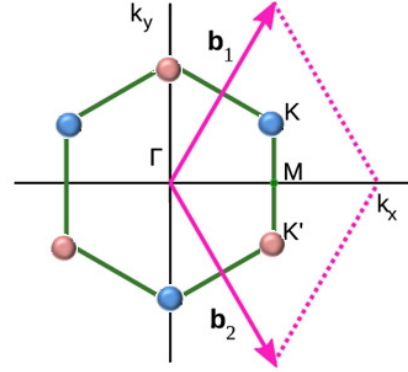


Figure 5 **a.** The Bravais primitive cell making up the honey-comb lattice and **b.** the first Brillouin zone for graphene. The lattice vectors are denoted by a_1 and a_2 . The blue and red atoms are the two carbon atoms located in the primitive unit cell. The reciprocal lattice vectors are represented by b_1 and b_2 . The parallelogram formed by a_1 and a_2 represents the unit cell. The K and K' are the reciprocal lattice intersection points and the distance $\frac{\sqrt{3}}{2} \Gamma$ -M is the carbon-carbon bond length.¹⁶

The primitive unit cell of graphene contains two equivalent atoms that, when the lattice is viewed as a whole, form two independent interpenetrating, crystalline Sub lattices A and B (Figure 6).

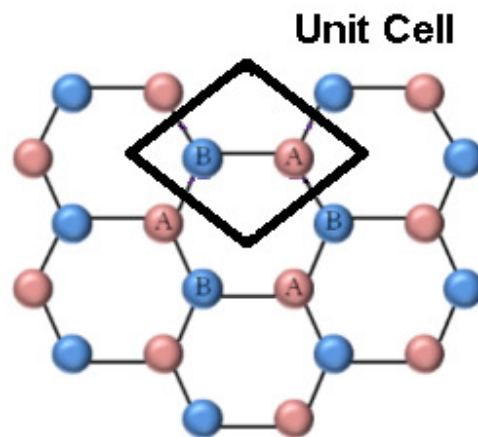


Figure 6. Showing the A - B pattern of sub lattices in graphene. A and B are both identical carbon atoms.

The structure, symmetry and lattice parameters described here are important when constructing a model of the band structure of graphene, as the dispersion relationship of the lattice is dependent upon the lattice and constituents of the lattice.

1.3 GRAPHENE DISPERSION RELATIONSHIP AND ELECTRONIC STRUCTURE

Electrons in the $2p_z^1$ orbital of individual C atoms form π -bands, and conduction occurs within these bands.¹⁰ In 1947, Wallace described the electronic structure of graphite using the tight-binding approximation,¹⁷ and calculated a band structure for a single atomic layer of graphite (i.e., graphene) predating the first direct experimental evidence by many decades. In a traditional semiconductor, the band structure near the Fermi level can be represented by the parabolic valence band and the conduction bands separated by a distinct energy gap. This can be pictured as per Figure 7, taken from Sighn.¹⁸ Graphene has a distinctly different dispersion relationship that is governed by the symmetry of the honeycomb lattice.

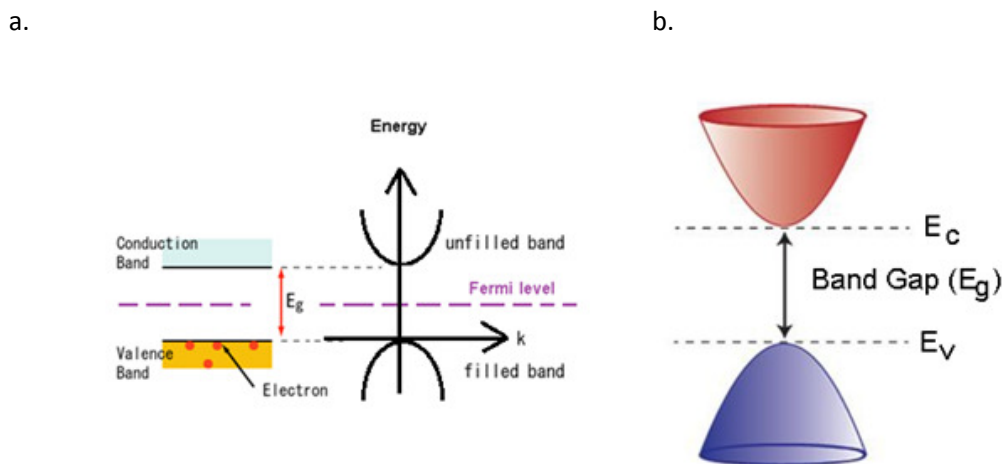


Figure 7. a. Showing band gap, E_g , of a typical semi conductor, E_g level encompasses the Fermi level and rests between E_c and E_v . The picture for a insulator is similar with the value of the Band gap (E_g) far greater than thermal energies of the electrons. b. Shows the band gap in momentum vector (k) space.

Neto et al.¹⁹ gave a comprehensive review of the electronic properties of graphene in 2009. The band structure of graphene is conical in shape at low energies near the corners of the Brillouin zone. This is represented in Figure 8b. The conduction and valence bands meet exactly at the K and K' locations. The Fermi level, in an undoped form of graphene passes exactly through these points. Figure 8a shows the three dimensional band structures over the whole unit cell.

The region of linear energy dispersion is referred to as the Dirac cone, and the intersection of the conduction and valence bands is known as the Dirac point. Figure 8b emphasizes the linear nature at the K points in crystal momentum space for small changes in energy ($\ll 1$ eV) around the contact of the valence and conduction bands. Hence, graphene is a zero band gap material with a linear dispersion relationship for small perturbations around the Dirac points.

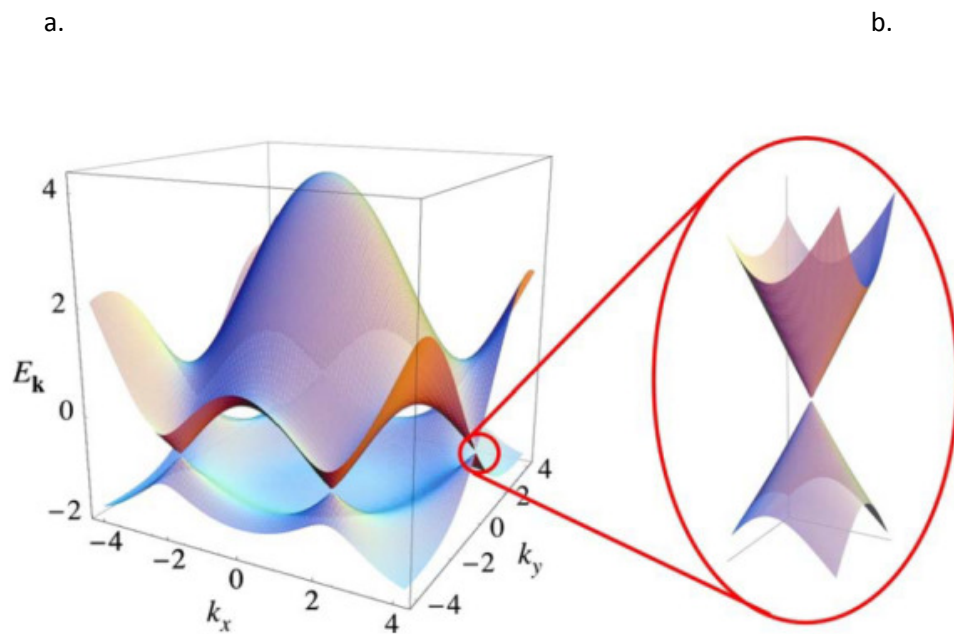


Figure 8.a. Energy diagram for graphene, the Energy $E_{\mathbf{k}}$ is given relative to the Dirac point; b. showing an expansion at the k point emphasising the linear nature of the Dirac cone. Diagram taken from Jorio et al.²⁰

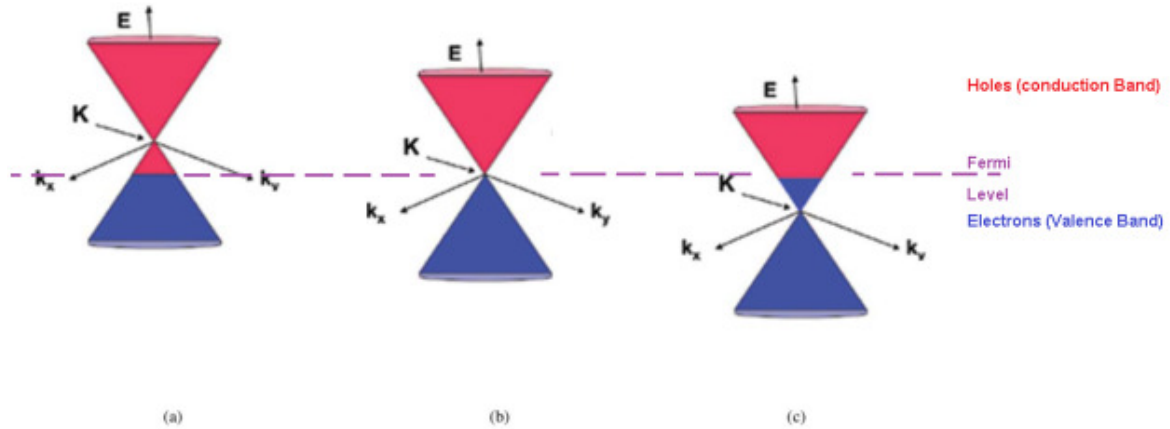


Figure 9. Shift in Fermi level as doping changes. In example (a), the graphene is positively doped, so the Fermi level is below the Dirac point. In example (b) the Fermi level crosses the Dirac point precisely; the graphene could be considered undoped whilst in example (c) the graphene is negatively doped meaning electrons exist above the Dirac point.

The energy dispersion E in k space is mathematically expressed as:

$$E = \hbar v_f \sqrt{(k_x^2 + k_y^2)}$$

where \hbar is Planck's constant divided by 2π , k_x, k_y represent the momentum vectors in the two dimensions, and v_f describes the Fermi velocity.

Geim et al.²¹ measured the Fermi velocity at approximately $1 \times 10^6 \text{ ms}^{-1}$, constant for both types of charge carriers in graphene. This linear energy dispersion has an analogy with photons, i.e., massless elementary particles that travel with constant velocity and also exhibit a linear energy dispersion relationship. The symmetry of the graphene lattice means that the energy of the electron-like and hole-like quasiparticle states in graphene have the same functional relationship on the k vector.

In order to construct a Bloch state which fully describe the conductance electrons in graphene within the tight bonding model, a linear combination of electronic wave functions localized at each carbon atom has to be constructed. Electrons from sublattices A and B contribute with the phase shift, which can be conveniently accounted for by introducing an additional degree of freedom – the pseudospin; the psuedospin can be thought of as similar to the spin in atomic descriptions.

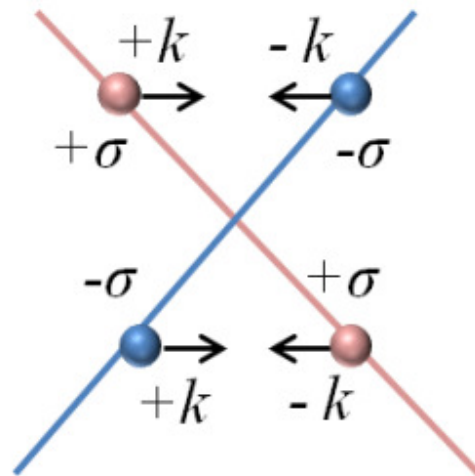


Figure 10a. Showing the spin (σ) and momentum vector k for each sub lattice A and B; colours as per Figure 9. Hence, 2 spins with 2 sub lattices means that each energy level is 4 fold degenerate.

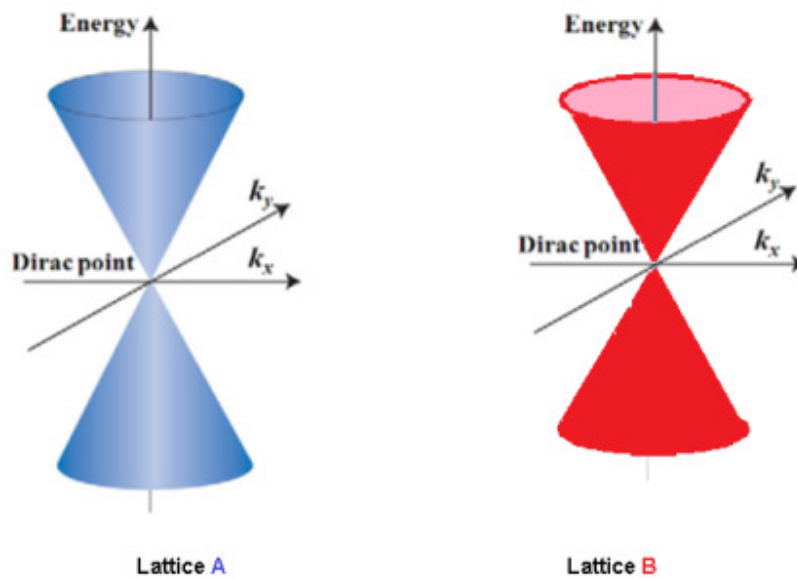


Figure 10b. The linear energy dispersion of graphene at the corners of the Brillouin zone. This cone is called the Dirac cone in the text. Each lattice A and B has a Dirac cone at the K points in the Bravais cell.

For this reason, the charge carriers in graphene are commonly referred to as Dirac fermions. Similarly, the region of linear energy dispersion is referred to as the Dirac cone, and the intersection of the conduction and valence bands is known as the Dirac point.

The symmetry of the graphene lattice and the introduction of the parameter pseudospin is another contribution to the superior conductivity of graphene. Charge carriers effectively hop between

sublattices during conduction, and as a result, these sublattices serve as a type of degree of freedom that is described by the pseudospin operator(σ).

1.4 Electron Transport Properties of Graphene.

The transport properties of graphene at low (non-quantising) magnetic field can be well described by using the Drude model. The charge carrier density is found by measuring the Hall effect. We define the x-y component of the resistivity tensor ρ as the Hall resistivity²²(R_{Hall}) which is given by:

$$R_{\text{Hall}} = \frac{-1}{ne} ; \rho_{xy} = \frac{B}{ne}$$

By applying an external magnetic field B perpendicular to the graphene sheet, the charge density of carriers ne , the transverse resistivity ρ_{xy} can be compared to the resistivity ρ_{xx} . At higher magnetic field strength B results in quantisation of electronic orbit and leads to the oscillation of the resistance (Shubnikov-de Haas oscillations) due to formation of many degenerate dispersionless states known as Landau levels, for low values of B the experiment can be used to find n , both in sign and magnitude.

At Higher magnetic field strengths, the Landau levels were measured and described by Nato et al.²³ by the relationship:

$$E_N = \pm v_f \sqrt{2Ne\hbar} \quad N = 0, 1, 2, 3 \dots n$$

This gives rise to the Half-Integer Quantum Hall Effect as E_N , energy of N th energy band is dependent upon $\sqrt{2N}$, ie the spacing of the energy levels decreases as N increases.

In comparison with Landau quantization in a 2D electron gas or 2D semiconductor, graphene represents a special case due to the previously identified linear dispersion. Therefore, we will first discuss the conventional Landau quantization, such that we are able to compare it with the quantization in graphene. Corresponding to these Landau levels, we consider in a second step the three types of Hall effect which we use to finally understand the anomaly of the QHE in graphene.

An electron experiences a magnetic flux quantum:

$$\Phi_0 = B\pi r_0^2 = \frac{h}{e}$$

with Φ_0 the magnetic flux for a unit cell of area πr_0^2 electron, charge e and h Plank's constant. To fully understand graphene: use of the Schrödinger Equation is preferred:

$$\frac{\left(\frac{\hbar}{i}\nabla - eA\right)}{2m_e}\varphi(r) = \varepsilon\varphi(r)$$

with m_e the mass of the electron and charge e , \hbar the reduced Plank constant, electrostatic potential A and energy ε for the solution of the wave function $\varphi(r)$.

Bloch allows the useful estimation of the wave function $\varphi(r)$, using the Born-Von Karmen boundary conditions for graphene of size l_{graphene} ; assuming graphene has a constant of thickness and is circular then:

$$\varphi(r) = \frac{c_{\text{graphene}}}{l_{\text{graphene}}} e^{ik \cdot r}$$

with c_{graphene} being a constant (inverse of thickness) as r is a repeated every Bravais primitive lattice cell; then

$$\varphi(r) = \varphi(r + R).$$

Switching to radial coordinates (r) for the above equation we have:

$$\frac{\hbar}{2m_e} \frac{d^2\varphi(r)}{dr^2} - \frac{1}{2} m_e \omega_c^2 r^2 \varphi(r) = \left(\varepsilon - \frac{\hbar^3 B_z^2}{2m_e}\right) \varphi(r)$$

That is

$$\varepsilon_n = (n + 1/2)\hbar\omega_c$$

The n^{th} energy level ε_n

From magnetic flux we have $B = \frac{\hbar}{er_0^2}$, the area r_0^2 , the unit cell length with field B and \hbar/e being Planks constant over electron charge. For a given B we can write the degeneracy as:

$$n_\phi = \frac{eB}{\hbar}$$

that is, as magnetic field increases the degeneracy increases. As the graphene unit cell has an area of $A_{\text{graphene unit cell}} = \frac{\sqrt{3}a_0^2}{2}$, with a_0 the carbon-carbon bond length, the ratio of magnetic flux to unit cell is:

$$\frac{B_n}{B_{unit\ cell}} = \frac{a_0^2}{r_n^2}$$

At the Dirac point the energy dispersion shows a zero point so the Landau levels will be of zero but still degenerate; 2 x for psuedospin and 2x for sublattice A and B making four-fold degeneracy.

At the Dirac point the uncertainty principle gives:

$$\partial E_{DP} \cdot \partial \left(\frac{1}{2\pi\omega_{DP}} \right) = \hbar$$

with a ω_{DP} equal to the ω_e from the Hall measurement giving a ∂E_{DP} of 0.5 eV; meaning the degeneracy of the central $n=0$ cannot be seen in graphene. Therefore the overall picture for the energy levels for graphene can be drawn as per Figure 11. The central peak in Figure 11 shows highest electrical resistance and consists of holes and electrons. Often it is more convenient to calculate the charge carrier density for plotting energy and resistance variation with B_n :

$$n = \frac{\epsilon_0 \epsilon_r V_g}{dq_e}$$

Where d is the thickness of the insulator layer of $\epsilon_0 \epsilon_r$ relative permittivity, the back gate at voltage V_g , q_e is the electron charge; given in this format to emphasise the capacitance of the system. In all cases $n \propto V_g$. Interesting, the Hall effect demonstrates that as the magnetic field B increases the density of states (per unit area) increases proportionally. The Landau levels provide more energy levels per unit area as the B field increases so experimentally at higher magnetic fields the ρ_{xy} increases.

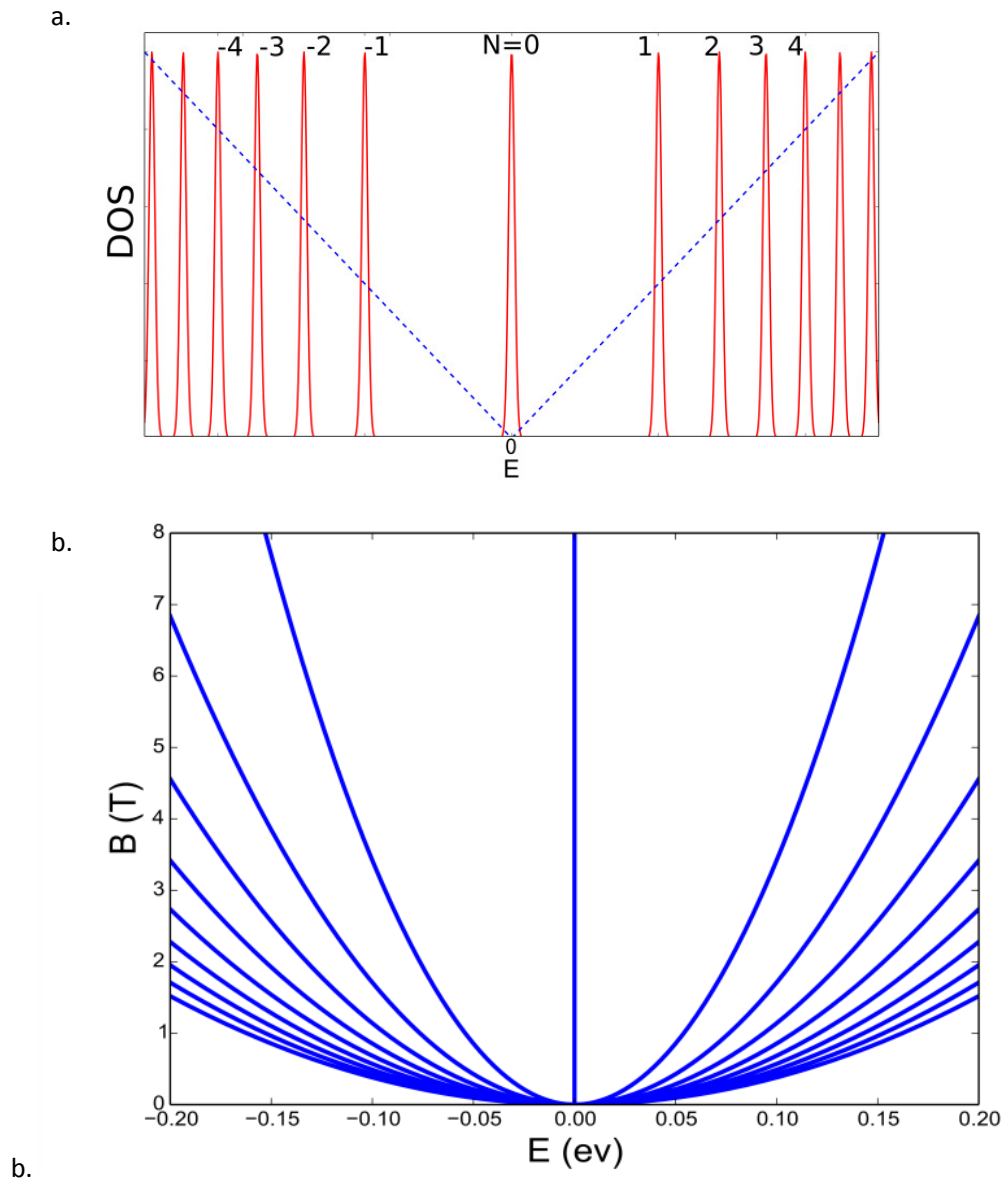


Figure 11. Graphene Landau levels and Quantum Hall levels taken from Zhang.²⁴ Figure (a) shows Density of States (DOS) with a plot of density of states vs. energy; the dashed lines show the density of states at zero magnetic field. Figure (b) shows the Landau level energy against magnetic field strength between 0 and 8 Tesla.

1.5 GRAPHENE SUPERLATTICE

Previously, we saw that electrons in a periodic crystal potential, such as graphene, leads to a measurable quantized energy spectrum, where the discrete energy bands are known as Bloch bands. In a magnetic field B_n the spectrum further splits into highly degenerate Landau levels with a relationship $B_n \propto 1/r_n^2$, as r_n^2 decreases the Landau levels broaden, taking on the form of bands, an effect described by Harper²⁵. At the quantized levels of r_n^2 the radius (energy) of the electron becomes integer with the unit cell area. In these cases, the magnetic field becomes equivalent of a discrete function of repetition n (unit cell), meaning that electrons follow the same behaviour in a magnetic field that resembles a "Magnetic translation group" exactly the same as the Bravais primitive cell. Zak²⁶ was able to conclude that:

$$\frac{\theta}{\theta_{BPC}} = \frac{p}{qa_{BPC}}$$

That is the ratio of magnetic flux θ is a integer fraction p/q . Notice that q is q x larger than the Bravais primitive cell.

Immediately, we can start searching for larger lattice constants so that lower θ_{BPC} can be used to probe higher fractions of the ratio p/q .

Hofstadter in 1973²⁷ took a square lattice and calculated the energy dispersion diagram for various magnetic fields. The pattern is presented in Figure 12.

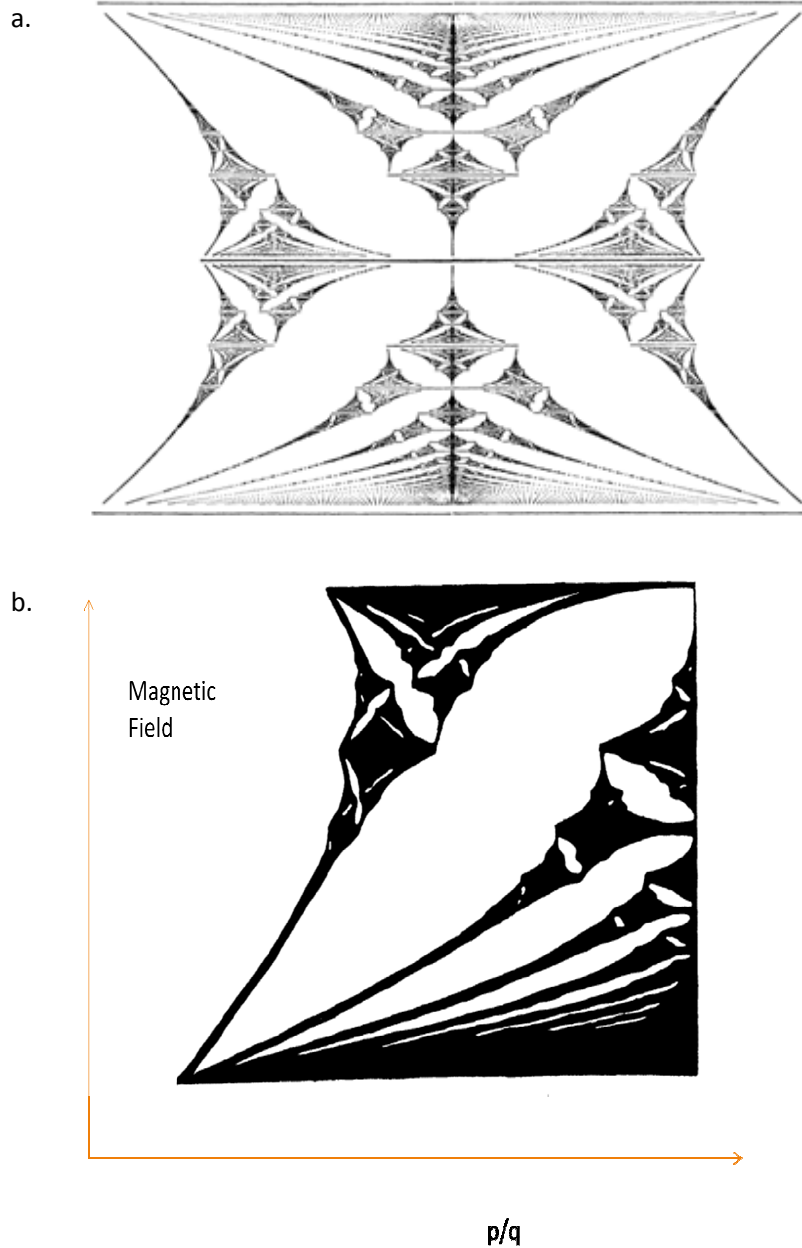


Figure 12. (a) The original figure of Hofstadter²⁷ showing energy (vertically) and p/q ratio horizontally. This picture is for a square planar crystal rather than a hexagonal graphene structure. The allowed energies are shown in black. (b) Effect of smearing on Hofstadter diagram; smearing of 1% of p/q leading to "bands" rather than fine scale. Taken from Hofstadter.²⁷ This calculated graph is more reflective of results obtained for resistance measurements in real samples.

The diagram in Figure 11 demonstrates the B field required to achieve a significant split that can be measured by variation in resistance; by the change in charge carriers. For graphene with a Bravais primitive cell, the area of the cell is 1.74 \AA^2 , meaning for $p/q = 1$, a magnetic field of approximately 105

Tesla would be required to observe a full spectrum as per Figure 12a. However, as Hofstadter proposed in his paper, a lattice of 10 nm would require approximately 50 Tesla to observe the whole spectrum. However, due to symmetry and the pattern self-replicating nature, a magnetic field of approximately 15 Tesla should be sufficient to experimentally map out the energy differences. Again, Hofstadter in his paper remarked that in a real experiment variations in P/q could lead to experimental uncertainty and fine detail lines would become broadened "bands" as per Figure 12b.

Hexagonal boron nitride.

Hexagonal boron nitride (h BN) is a III-V equivalent of carbon; the Bravais primitive cell has the same symmetry as graphene. The bond length is just 2% different to that of graphene with a boron-nitrogen bond length of 0.145 nm. Careful co-alignment of graphene and h BN crystals leads to the development of a Moiré pattern as illustrated in Figure 13. The new psuedo crystal pattern has a crystal lattice parameter of L_{sl} :

$$L_{sl} = \frac{a_{graphene}}{\sqrt{2(1 - \partial_{g-hBN})\sin\phi + \partial_{g-hBN}^2}}$$

the two lattices may have different orientation, which is determined by the mis-orientation angle ϕ . The difference between the two wave vectors of the graphene and h-BN lattices leads to the appearance of a hexagonal superlattice structure, with ∂_{g-hBN} being the difference between the lattice crystal of graphene, $a_{graphene}$, and that of the lattice constant of hexagonal Boron Nitride.

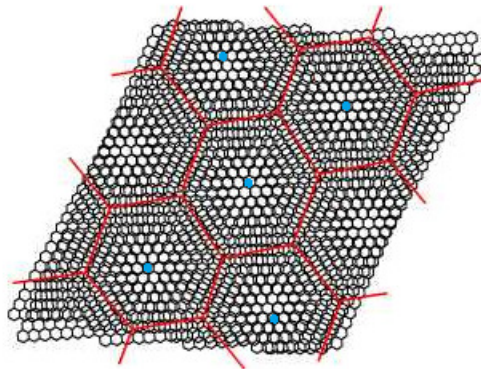


Figure 13. Showing Moiré pattern of graphene on h BN with 5° mis-alignment for legibility. Blue (hexagons) show macro-psuedo crystal centres at ca. 1.31 nm centres whilst the redlines show regions of maximum mis-match of the graphene and h BN. The pseudo-crystal Moiré pattern has the same symmetry as the graphene and h BN. Adapted from Hunt.²⁸

The new psuedocrystal has an energy dispersion relationship as seen in Figure 14 with a more detailed view given in Figure 14b.

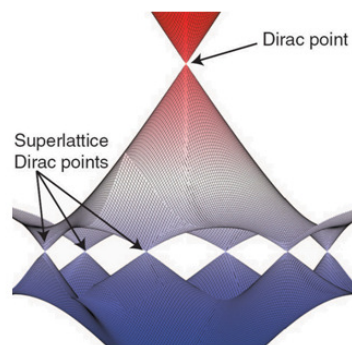
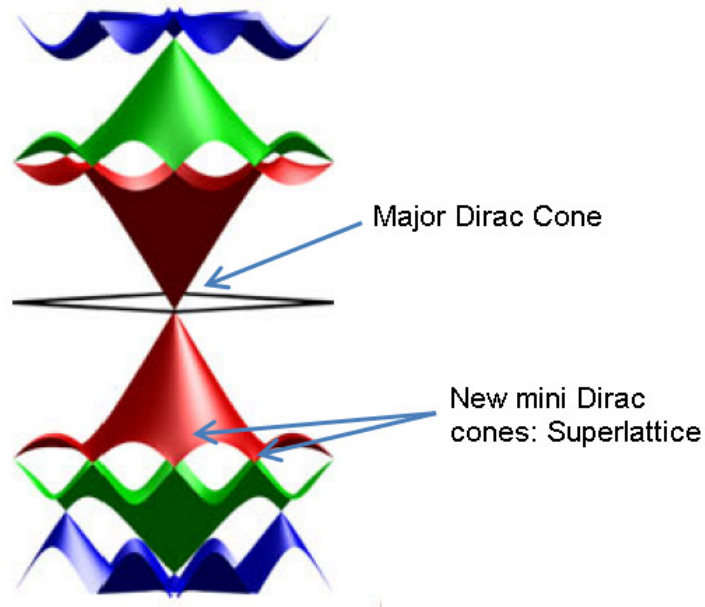


Figure 14. (a) Formation of Multiple Dirac cones with graphene on hexagonal Boron nitride. (b) Close up of the lower energy (new) superlattice Dirac cones of graphene-hBN superlattice. Notice the symmetry; the same as that as graphene and h-BN. Taken from Falko.²⁸

The large, psuedo, moiré crystal made up of the carefully aligned graphene-h boron nitride means that the length of the primitive (psuedo) crystal is ca. ten fold larger than the crystal Bravais cell of graphene, meaning that the required magnetic field to achieve a clear pattern for the Hofstadter pattern is 100 x

smaller, allowing measurements to be made at 10-20 Tesla. In the experimental set used within this work a magnetic field of 15 Tesla is used, allowing access of the Wannier²⁹ diagram.

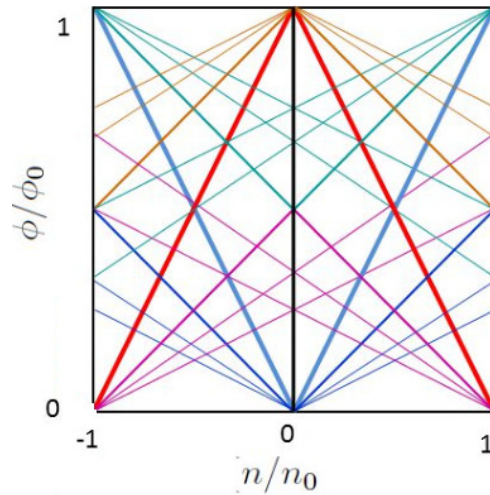


Figure 15a Wannier diagram for graphene. Lines represent energy gaps in the spectrum. Resistance is larger when the Fermi level lies within the larger gaps corresponding to thicker lines on the diagram. Taken from Wannier.²⁹

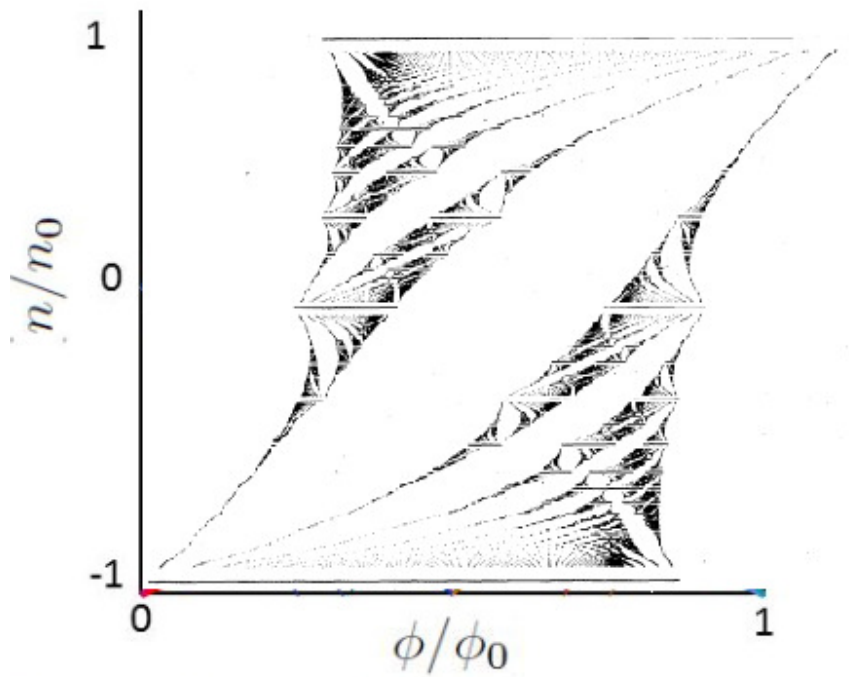


Figure 15b. Wannier calculation for a hexagonal lattice (such as graphene) which shows an asymmetrical arrangement of magnetic bands for Φ/Φ_0 0 to 1. Adopted from reference 30.

The symmetry of graphene and h-boron nitride is $p6$; that is triangular in nature. Wannier³⁰ calculated the symmetry difference for a triangular (hexagonal) lattice and this is reproduced in Figure 15.

1.6 CONCLUSION AND SUMMARY

Starting from the graphene structure and careful observation of literature on graphene dispersion relationships we have arrived at a method for observing fine scale quantum effects using moderately high, yet accessible magnetic fields available within Lancaster Physics Department.

The ability to study the fine scale quantum properties, such as psuedo spin and Landau level distribution allows hypothesis of quantum physics and understanding to be tested with accessible experimental structures.

1.7 REFERENCES

-
- ¹ H. P. Boehm, R. Setton, and E. Stumpp, *Pure and Applied Chemistry*, vol. 66, pp. 1893-1901, Sep. 1994, "Nomenclature and terminology of graphite-intercalation compounds."
- ² J. D. Bernal, B. A., Published 1 December 1924. *Proceedings of the Royal Society A*. "The structure of graphite."
- ³ P. R. Wallace, *Physical Review*, vol. 71, pp. 476476, 1947, "The band theory of graphite."
- ⁴ J. C. Slonczewski and P. R. Weiss, *Physical Review*, vol. 71, pp. 476476, 1947, "Band structure of graphite."
- ⁵ A. J. Vanbommel, J. E. Crombeen, and A. Vantooren, "LEED and Auger-electron observations of SiC (0001) surface," *Surface Science*, vol. 48, pp. 463-472, 197
- ⁶ N. D. Mermin, "Crystalline order in 2 dimensions," *Physical Review*, vol. 176, pp. 250-254, 1968.
- ⁷ E. Fradkin, *Physical Review B*, vol. 33, pp. 3263-3268, Mar. 1986, "Critical-behavior of disordered degenerate semiconductors II - Spectrum and transport properties in mean-field theory."
- ⁸ K. S. Novoselov, A. K. Geim, S. V. Morozov, D. Jiang, Y. Zhang, S. V. Dubonos, I. V. Grigorieva, and A. A. Firsov, *Science*, vol. 306, pp. 666-669, Oct. 2004, "Electric field effect in atomically thin carbon films."
- ⁹ P. Blake, K. S. Novoselov, A. H. Castro Neto, D. Jiang, R. Yang, T. J. Booth, A. K. Geim, E. W. Hill. *Appl. Phys. Lett.* 91, 063124, (2007). "Making graphene visible."
- ¹⁰ W. J. Smith. *Modern Optical Engineering - The Design of Optical Systems*. 3rd Edition, McGraw-Hill, 2000, section 5.3.
- ¹¹ K. S. Novoselov, D. Jiang, F. Schedin, T. J. Booth, V. V. Khotkevich, S. V. Morozov, and A. K. Geim, *Proceedings of the National Academy of Sciences of the United States of America*, vol. 102, pp. 10451-10453, Jul. 2005, "Two-dimensional atomic crystals."
- ¹² P. Blake, E. W. Hill, A. H. Castro Neto, K. S. Novoselov, D. Jiang, R. Yang, T.J. Booth, T. A.K. Geim, *Appl. Phys. Lett.* **91**, 063124 (2007).
- ¹³ S.J. Blanksby and G.B. Ellison, *Acc. Chem. Res.* 36 (4), 2003, pp. 255–263, "Bond Dissociation Energies of Organic Molecules."

-
- ¹⁴ A. K. Geim and A. H. MacDonald, *Physics Today*, vol. 60, pp. 35-41, Aug. 2007, "Graphene: Exploring carbon flatland."
- ¹⁵ R. Zacharia, H. Ulbricht, T. Hertel, *PHYSICAL REVIEW*, 2004, B 69, pp. 155406, "Interlayer cohesive energy of graphite from thermal desorption of polyaromatic hydrocarbons."
- ¹⁶ N. Kerszberga and P. Suryanarayana. *RSC Adv.*, 2015, 5, pp. 43810.
- ¹⁷ P. R. Wallace, *Physical Review*, vol. 71, pp. 476476, 1947, "The band theory of graphite."
- ¹⁸ J. Singh, *Electronic and Optoelectronic Properties of Semiconductor Structures - Chapter 2 and 3*, ISBN 0-521-82379.
- ¹⁹ A. H. Castro-Neto, K. S. Novoselov and A. K. Geim, N. M. R. Peres, F. Guinea, *Reviews Of Modern Physics*, Volume 81, January–March 2009, "The electronic properties of graphene."
- ²⁰ A. Jorio, M. S. Dresselhaus, R. Saito, G. Dresselhaus ISBN: 978-3-527-40811-5. "Raman Spectroscopy in Graphene Related Systems."
- ²¹ K. S. Novoselov, A. K. Geim, S. V. Morozov, D. Jiang, M. I. Katsnelson, I. V. Grigorieva, S. V. Dubonos, and A. A. Firsov, *Rev. Mod. Phys.*, 81 (2009), pp. 109-162. "Two-dimensional gas of massless Dirac fermions in graphene," and *Nature*, vol. 438, pp. 197-200, Nov. 2005.
- ²² E.H. Hall, 1879, *American Journal of Mathematics* 2(3),pp. 287.
- ²³ A.H. Castro Neto, F. Guinea, N.M.R. Peres, K.S. Novoselov, A.K. Geim, *Rev. Mod. Phys.*, 81 (2009), pp. 109-162. "The electronic properties of graphene."
- ²⁴ Y. Zhang, Y.-W. Tan, H. L. Stormer, and P. Kim, 2005, *Nature* 438(7065), pp. 201.
- ²⁵ P.G. Harper. *Proc. Phys. Soc. Sect A***68**, pp. 874, (1955). "Single Band motion of Conduction Electrons in a Uniform Magnetic Field."
- ²⁶ J. Zaq, *Phys Rev.* **134**, A, pp. 1602-1606 (1964), "Magnetic Translation Group."
- ²⁷ D. R. Hofstadter. *Phys. Rev. B* **14**, pp. 2239-2249, 1976. "Energy levels and wave functions of Bloch electrons in rational and irrational magnetic fields."
- ²⁸ J. R. Wallbank, M. Mucha-Kruczyński, Xi Chen, and V. I. Fal'ko. *Ann. Phys. (Berlin)* 527, No. 5–6, pp. 359–376, (2015). Moiré superlattice effects in graphene/boron-nitride van der Waals heterostructures
- ²⁹ G. H. Wannier, *Phys. Stat. Sol. (b)* 88 , pp. 757–765 (1978).

³⁰ F. H. Claro and G. H. Wannier. Phys. Rev. B 19, 1979, pp. 6068. "Magnetic subband structure of electrons in hexagonal lattices."

CHAPTER 2. RAMAN SPECTRAL ANALYSIS.

2.1 INTRODUCTION

In this section the Raman theory is reviewed with respect to the type of characterisation undertaken with graphene. Thereafter, the analysis of the Raman spectra of prepared graphene flakes is presented. The tested flakes were obtained in order to analyse purity of the graphene in a non-destructive manner. After the Raman analysis, graphene flakes were processed further to make Hall bars. Wherever possible, the Raman spectra were obtained in such a manner to avoid laser damage to regions of interest, thus allowing samples to be used in further studies and fabrication steps.

2.2 RAMAN THEORY

When light interacts with graphene, the light energy can be either absorbed or scattered. If the light is scattered this can be either in an elastic or inelastic manner. Raman scattering is an inelastic process. From the macroscopic viewpoint an incoming photon is scattered at the graphene lattice. This process induces a phonon in the solid and reduces the energy of the exit photon by the energy lost in the scattering event. However, this description implies a direct interaction of the photon and the phonon. Classically, a photon-phonon energy exchange is very improbable; whilst from a quantum mechanical perspective Aharonov and Bohm¹ formulated a photon matter interaction that was latter experimentally verified. More evidence is available for the interaction of light with electrons and electrons with phonons; that is the basis of the Raman effect as a two process phenomena. The Raman process involves the excitation of an electron.

Raman spectroscopy belongs to optical analytical spectroscopy, and in particular is related to optical inelastic scattering of light. It was discovered by C.V. Raman in 1928.² Rayleigh scattering, discovered by Strutt³ by contrast, is a process of elastic energy conservation. In any Raman experiment, Rayleigh scattering needs to be accounted for in the detection system. In order to obtain good Raman signals, Rayleigh scatter from the sample needs to be blocked with an efficient, (very) narrow band filter. The Rayleigh scattering occurs at the wavelength of the incident energy hence a Rayleigh blocking filter is placed in the light path after the sample irradiation and before signal detection. See Figure 18 for a qualitative description of the Rayleigh and Raman energy transitions that are responsible for Raman observation. Figure 19 gives the experimental set up used for a typical microscopic Raman experiment.

In the experimental set up described in this work two different laser frequencies are available as excitation sources:

1. 514 nm Green 5 mW 8 micron spot size.
2. 612 nm Red 1 mW 10 micron spot size.

Taking a classical approach to describe the Raman phenomena, the incident radiation has an electric field strength that interacts with the graphene electron gas cloud: the induced dipole μ (electron-hole separation of Figure 17) can be described as:

$$\mu = \alpha E_0 (\cos \omega_1 t)$$

where α is the graphene polarisability, E_0 , the electric field strength at $t = 0$ and has an incident frequency ω_1 . From Figure 16 it can be observed that the graphene polarisability α changes with crystal momentum space $k(r)$ in a linear manner to a first approximation for small changes in $k(r)$, a reasonable assumption as vibrations are only a small fraction of the interatomic distances in graphene.

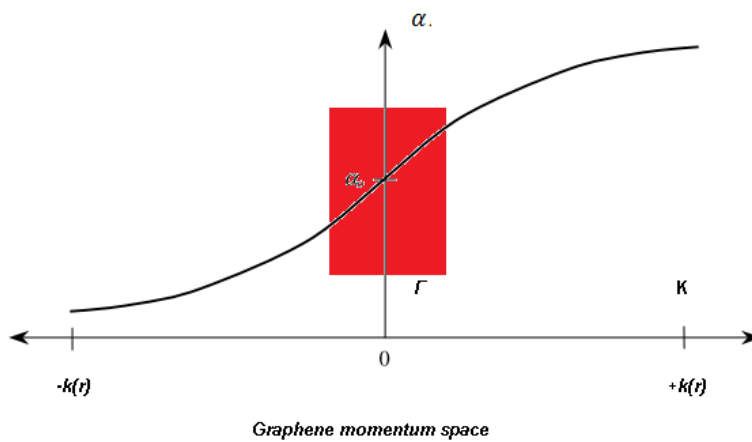


Figure 16. Change of polarisability α with graphene crystal moment space. Near Γ (the region in red) $\delta\alpha/\delta k(r)$ is constant.

$$\alpha = \alpha_{k(r)=0} + \left(\frac{\delta\alpha}{\delta k(r)} \right) q$$

with $q = q_0 \cos(2\pi\omega_R t)$ (q_0 at $t = 0$)

where ω_R is the Raman Frequency of the phonons and q, q_0 is the instantaneous electric field strength and at $t = 0$ respectively. The term ω_R is derived from the quantum term for vibrational frequency.

Together this gives:

$$\mu = \alpha_{k(r)=0} E_0 \cos(2\pi\omega_0 t) + q_0 E_0 / 2 \left(\frac{\delta\alpha}{\delta k(r)} \right)_{k(r)=0} [\cos 2\pi(\omega_I + \omega_R)t + \cos 2\pi(\omega_I - \omega_R)t]$$

i.e. Rayleigh scatter, Raman stokes and Raman anti-stokes frequencies.

The vibration energy E_{Raman} of a particular Raman mode is given by:

$$E_{Scatter} = h\omega_R \left(J + \frac{1}{2} \right) \text{ with } J = 0, \pm 1, \pm 2, \pm 3 \dots$$

With most typical Raman vibrations of frequency ω_{Raman} being for $J = +1$ (the first excited state), For anti-Stokes $J = -1$, $J = 0$ is the case for Rayleigh scattering.

The conservation of momentum of the excitation light source can be considered via a Feynman diagram for Raman as shown in Figure 17.

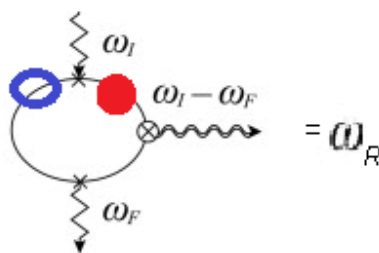


Figure 17. Feynman diagram for a simple Raman process. Incoming photon of frequency ω creates an electron-hole pair; denoted by solid circle and ring respectively. A phonon travelling in the crystal graphene mixes with the electron-hole pair exchanging momentum. The electron-hole recombine and the photon is eliminated with frequency ω_f . The phonon in the crystal has frequency ω_R , the Raman frequency.

The signal is very dependent on the symmetry and structure of the ground and “excited” states. These general signal are called Stoke lines and in this analysis only the Stokes lines are observed. The anti-stokes lines would require an optical filter with cut-off at higher frequency (short pass/notch filter) rather than a long pass filter to eliminate Rayleigh scattering. As anti-stokes lines are of higher frequency, using the Boltzman distribution:

$$N_e = \frac{g_e}{g_o} N_o \exp\left\{\frac{-\partial E}{k_B T}\right\} \quad \text{Equation 1}$$

In this case, N_e is the population of the first vibrational excited state, N_o is the population of the ground state, $\frac{g_e}{g_o}$ is the ratio of the degeneracy of the excited state and of the ground state respectively, with ∂E being the energy difference between the excited vibrational state (E_e) and the energy of the ground state (E_o), with k_B as the Boltzmann constant, and T is the temperature of the electrons in the material. Temperature is an most important parameter to understand: as lasers can cause intense local heating leading to changes in N_e/N_o . As N_e/N_o increases the intensity of the Raman signal will decrease.

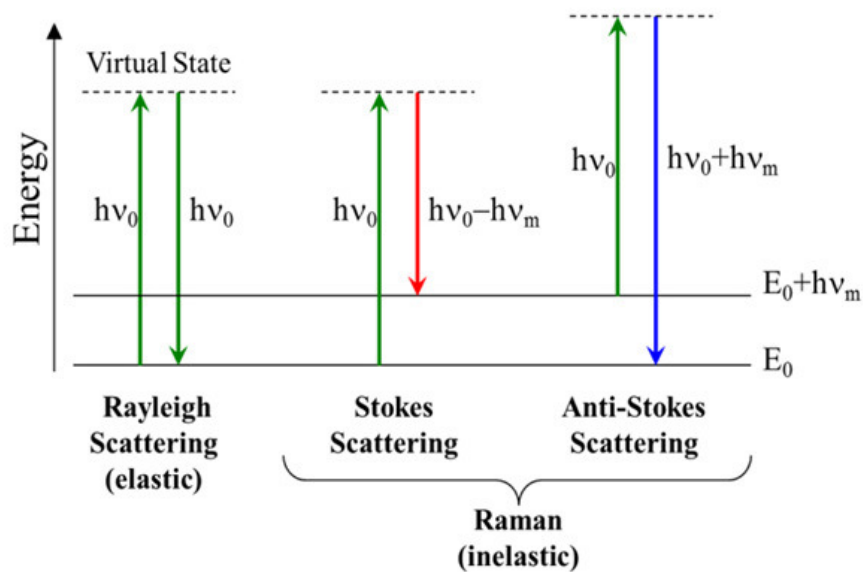


Figure 18. Simplified energy diagram for processes occurring in Rayleigh and Raman scattering.

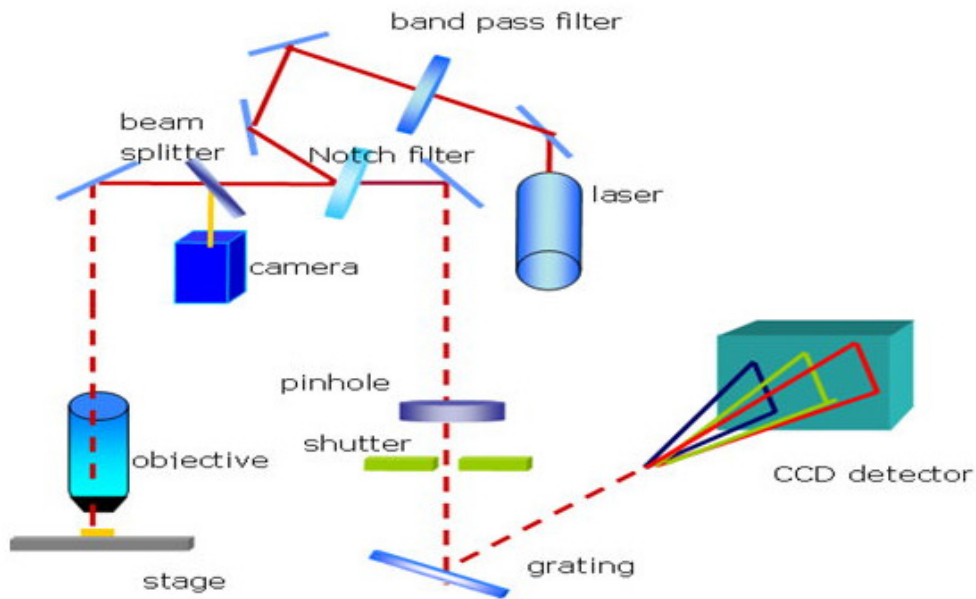


Figure 19. Simplified sketch of the Raman microscope used to analyse graphene fragments.

The intensity of the Raman scattering is a product of the probability of the excitation and emission of the photon:

$$I_{\text{Raman}} \propto \alpha_I \alpha_{\text{scatter}}, \alpha \sim \alpha^2$$

i.e. the intensity of the Raman signal I_{Raman} is proportional to the square of polarisability.

The position of the Raman scatter (phonon) and the intensity of the scattering allow the structure of graphene to be compared. The energy of the lines observed is reported as inverse wavenumbers (cm^{-1}) and the position of the lines give indications of the energy changes within the system. Intensity changes give indications of changes especially of symmetry and charge distribution. With graphene Raman symmetry and charge distribution can be the result of poor samples or poor sample handling giving rise to doping (impurity), tears, wrinkles or multi stacks.

Since graphene is a broadband absorber,⁴ approximately 2% of all light from IR to near UV is absorbed, there is a secondary interesting phenomena that occurs with graphene and Raman spectroscopy. Normally, the incident radiation may, or may not be absorbed by the material so the electron-hole excitations are virtual. However, since graphene is a broad band absorber any (visible) laser source radiation will be absorbed by the graphene. The result is that the electron-hole separation in the excited state from the laser has a finite lifetime, much longer than a virtual excited state. This results in

a far higher number of absorptions of the incident laser than for the excited states than for a non-absorbing sample, this leads to an enhanced Raman signal. This can be thought of as resonant Raman spectroscopy. As the intensity of the signal (scattering) is much higher, a lower power (laser) and shorter integration time to obtain an adequate signal to noise ratio is required. This is useful for graphene analysis since the samples will be used for device fabrication: intense laser irradiation will cause graphene lattice damage (vide infra).

2.3 GRAPHENE RAMAN EXPLANATION.

Graphene was first characterised by Ferrari⁵ using Raman to understand the structure and impurities present in n-layer graphene (n= 1, 2,3 ...). Raman has now ubiquitous use as the preferred method of graphene (mono) layer structure analysis; it is relatively quick and if performed carefully relatively non-destructive. Ferrari noted that great care was needed to avoid laser damage to graphene samples.

Intense laser power or extended exposure time causes graphene changes to structure possibly due to:

1. Heating effects on graphene or of substrate.
2. (Photo)Oxidation of graphene
3. Contamination from air/substrate.

Some workers, such as Moshkalev,⁶ have used laser illumination to alter graphene materials. Hence, in the work presented here, whenever a Raman spectrum was taken careful planning of sample region of laser illumination was undertaken to prevent unnecessary damage to regions of interest.

2.4 GRAPHENE RAMAN PEAKS FOR IDENTIFICATION.

There are four peaks of interest in identifying graphene as a monolayer. In Figure 20 three of these can be easily observed even when a low signal to noise spectrum is obtained. In this section the peaks will be identified, described and demonstrated how they verify the presence of graphene.

The first peak of interest in the Raman spectrum is the so called "Graphite" peak (labelled G in Figure 20).

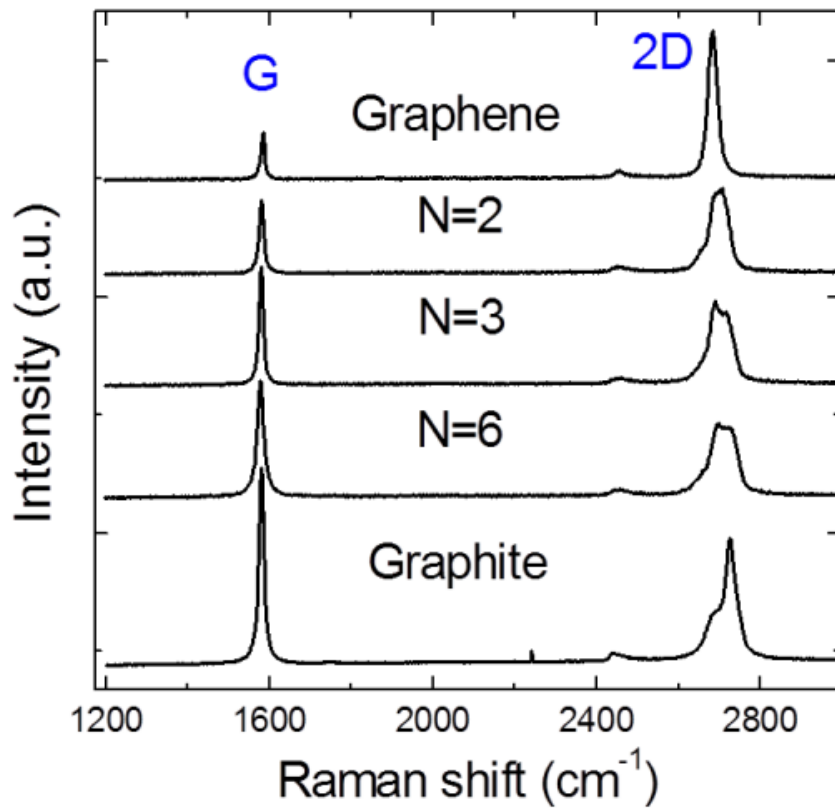


Figure 20. Graphite, multi layer graphene and graphene Raman spectrum overlaid to show changes of Raman spectra versus number of graphene layers.. The graphene (G) peak at 1500 cm^{-1} and the 2D (doped) at 1600 cm^{-1} are typical for a planar 2D graphene material. Note the ratio of the two main peaks and the relative peak heights/areas (intensity). Adapted from Saleh.⁷

The G peak of the Raman spectrum of graphene is present in all sp²-bonded carbon systems and is named after "Graphite." The G peak is generated by incident photons scattering off (electrons) transverse in-plane vibrations of the lattice as per figure 21. The peak is located at a Raman shift of approximately 1585 cm^{-1} with a full width at half maximum of about 13 cm^{-1} . The G peak intensity is very sensitive to changes in the environment of a graphene layer, see Figure 20.

The G peak and 2D peak are the only active Raman bands since these two modes of phonon action induce a polarisation. The G peak is the simplest peak as the excitation and emission take place within the same Dirac cone. An energy diagram for the G, D and 2D peaks is presented in Figure 22.

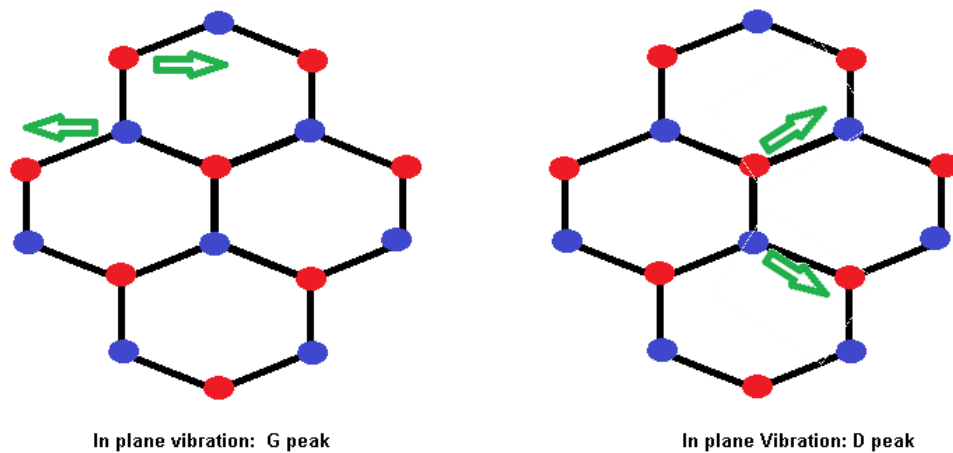


Figure 21. The two vibrations leading to changes in polarisability in a 2D crystal such as graphene; the G peak is called stretching "graphite" and the D peak is called "breathing". Both are in plane; out of plane vibrations only occur when the graphene structure is twisted or bent out of a 2D plane.

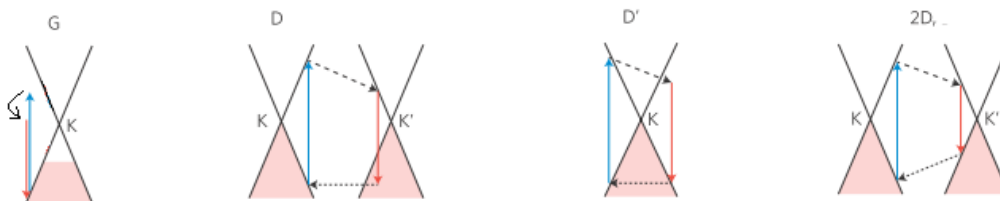


Figure 22. The main Raman active peaks for graphene, G, D, D' and 2D. In all cases momentum and spin have to be conserved; hence the vector directions of the arrows are as per a Feynman diagram. The Dirac cone is not to scale, the optical transitions are 2eV (approximately) whilst phonon (vibration) transitions are 10meV. Taken from reference 8.

The utility of Raman spectrometry for graphene that is of poorer quality is illustrated in Figure 23; the D and D' peaks are comparable in intensity to the G and 2D peaks. The graphene in this instance is very poor quality; the spectrum is presented so that assignment of graphene with defects can be unambiguously assigned. In particular the mixing of D and D' prime and the appearance of a 2D' peak are clear indications of poor quality graphene. A simple explanation for the increase in number of peaks is the decrease in symmetry and increase in scattering centres as the perfect graphene crystal becomes

distorted. For graphene, the G band and the 2D band offer fast conformation of monolayer formation and the G and D (D') peak offer insights into doping and quality of the graphene substrate.

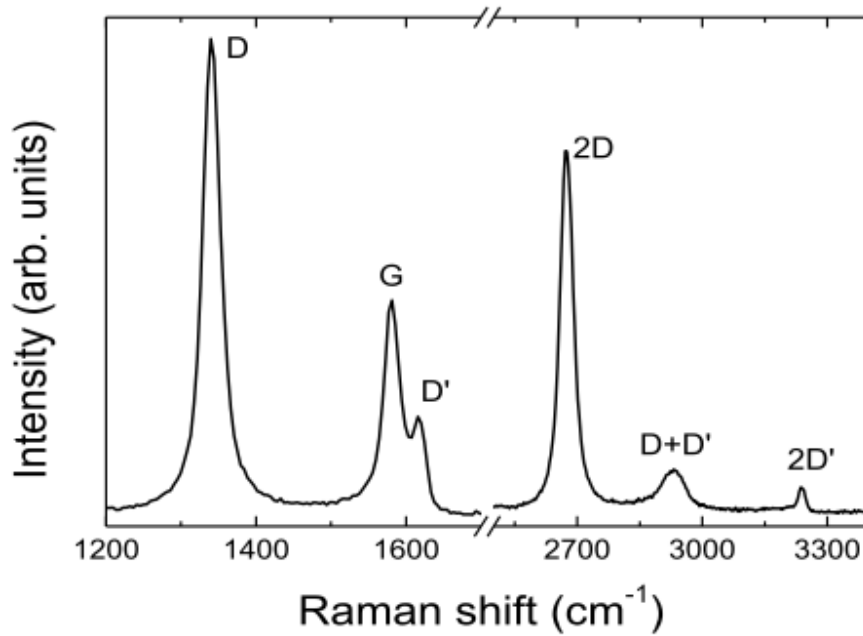


Figure 23. Raman spectrum of highly defect concentration graphene. Taken from Ferrari.⁵

2.5 RAMAN ANALYSIS.

In this section, the spectra of samples are presented followed by tabular analysis.

Spectra 1. CVD graphene (ex commercial)

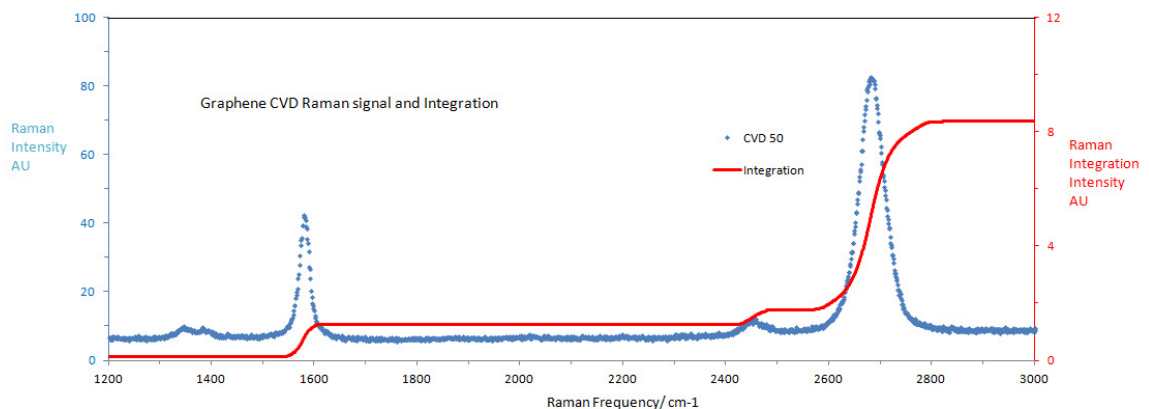


Figure 24. Raman spectrum of CVD graphene taken at 514 nm.

Table1. Data of Raman Spectroscopy data for flake testing.

Sample/ Figure	D peak	G Peak and integration	G' (second order) (FWHM)	2D Peak and integration	2D Peak Width/ (Lorentz FWHM) $25 \text{ cm}^{-1} = 3$ meV	2D:G Integration (Intensity) ratio
	/wavenumber cm^{-1}					
CVD	1344 (1.12)	1585 (2.30)	2452 (53)	2682 (14.9)	56	6.5 (2.7)
Flake 4		1589 (2.35)	2457	2686 (19.1)	25	8.3 (2.6)
Flake 5		1583 (1.62)	2458	2708 (22.5)	66	5.7 (1)
Bilayer	1344 (1.11)	1585 (1.70)	2452 (68)	2699 (12.2)	66	7 (1)
Thick		1583 (9.7)	2456	2722 (465)	90	4.8 (0.7)
Single		1585 (2.49)	2455 (24)	2686 (19.5)	27	7.8 (3)
Attached		1588 (0.83)	2451	2682 (7.86)	28	9.5

2.6 RAMAN ANALYSIS OF PRESENTED SPECTRA

In this section the Raman spectra collected are analysed sequentially; spectra represent the types of graphene used in this work; both mechanical "scotch tape" and CVD graphene.

A brief description of the peak fitting process will be given. The data obtained from the Raman spectrometer is the raw data from the ADC from the sensor chip. The ADC sensor combination has an offset of ca. 140 (units) with a signal to noise ratio of ca. 0.17. The offset can be considered a dark current-bias with the standard deviation being the sensor circuitry instability. With a spectral resolution of 0.97 cm^{-1} (0.12 meV) this is far smaller than "thermal" equilibrium noise of ca 200 cm^{-1} (KT) at 295 K. To smooth the data a simple "rolling" sum of 9 data readings is taken. This procedure allows more accurate location of the peak via the derivative of the signal with respect to wavenumber. The signal is then modelled with a Lorentzian fit until a good fit (<1 %) variation of collected data to modelled data is obtained. The Lorentzian model can then be used to directly find the FWHM of the particular peak. The

data can also be used to integrate the peak area to find peak area ratios, for example of G and 2D peaks as presented in Table 1.

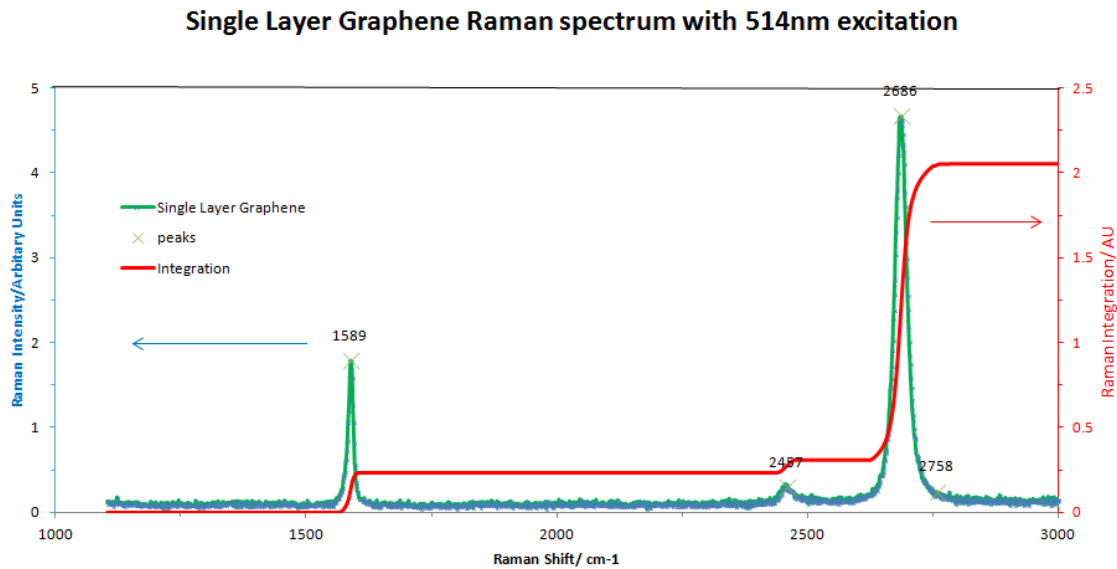


Figure 25. High quality "single layer" graphene from mechanical exfoliation. The excitation wavelength was 514 nm, this is Flake 5.

The single layer graphene Raman spectrum shown in Figure 25 shows a 2D peak at 2686 (+/- 1) cm⁻¹ fully consistent with other workers including Ferrari¹⁰ noting that the 2D peak was observed at 2685 cm⁻¹. The FWHM of 27 (+/- 2) cm⁻¹ of the single layer is entirely consistent with monolayer graphene and is also symmetrical.

The integration ratio of the 2D and G peaks as well as the FWHM, calculated from a Lorentzian line shape, are presented in Table 1. Optical observation of flake 5 indicated a monolayer, based upon colour on a silicon dioxide layer; however, Raman analysis strongly indicates that flake 5 is a bilayer structure whilst flake 4 is in fact a monolayer. Optical recognition of single, or double layers is good when comparing samples, however, with isolated flake, comparison can be harder sometimes leading to inaccurate assignment of structures. Addition of glue or contamination on a surface can lead to incorrect assessment of graphene layer number as the optical "colour" or path length may change altering the assignment.

Raman analysis from peak position, peak intensity and peak shape provide a consistent verification of monolayer graphene. A typical monolayer has a peak around 2675 to 2685 cm^{-1} for the 2D peak, and around 2450 cm^{-1} for the G peak. The FWHM of the 2D peak is ca. 25-29 cm^{-1} . Clearly, FWHM widths of two or three times this value indicate multiple peaks (2-3 overlapping peaks) rather than a single "pure" peak of mono layer graphene.

The CVD graphene (methane and hydrogen synthesis over copper) gives a good agreement for the 2D peak position but shows broader peak FWHM than for single graphene from exfoliation route.

The 2450 cm^{-1} peak is related to the G peak and as per Shinohara¹¹ is classed as non-dispersive as the 2450 cm^{-1} band is invariant with excitation energy. Saito¹² showed that the G' peak is an inelastic phonon transfer and for G' at 2540 cm^{-1} the process is symmetrical, for the G peak the process is asymmetric. It was hoped that the G' peak analysis would lead to clearer identification of graphene 2D materials. The reduced intensity (20-100 times less) compared to the G peak makes accurate measurement of G' less useful. Interestingly, the CVD grown graphene shows a significantly different G' peak (blue shifted) with a FWHM of approximately twice that of monolayer graphene.

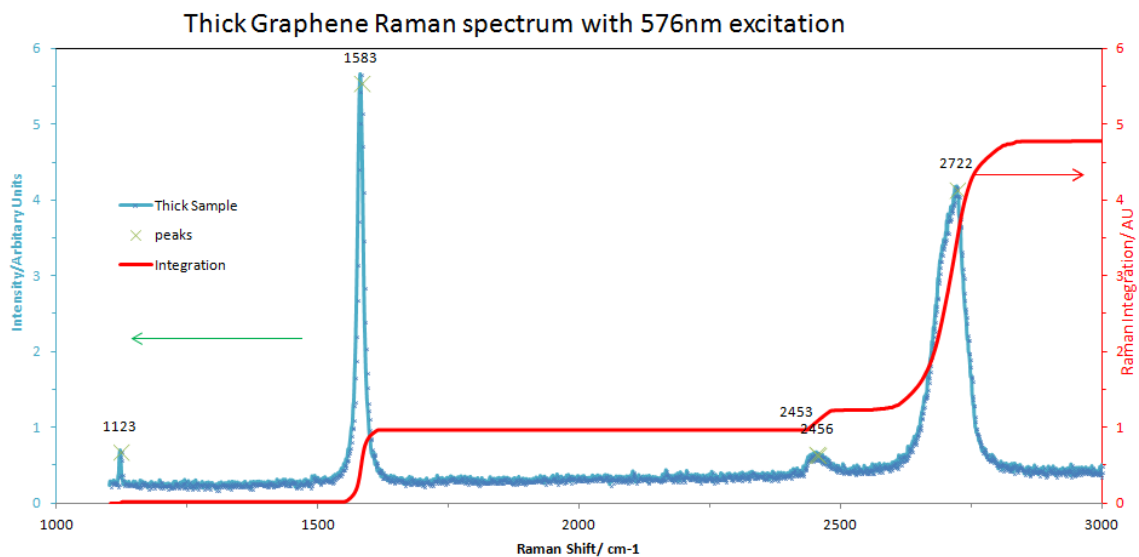


Figure 26. Thick graphene (many layers) or thin graphite to compare signal response. Sample clearly shows broadening of 2D peak and very large G peak.

Figure 26 shows the Raman spectrum of multi layer graphene (or thin graphite). The 2D peak can clearly be seen to have a much greater FWHM whilst the graphite peak (G) is considerably enhanced in intensity. Also from figure 26 the G' peak is more pronounced. The 2D peak is considerably blue shifted to higher frequency by over 50 wave numbers compared to single layer graphene.

Bilayer Graphene Raman spectrum with 576nm excitation

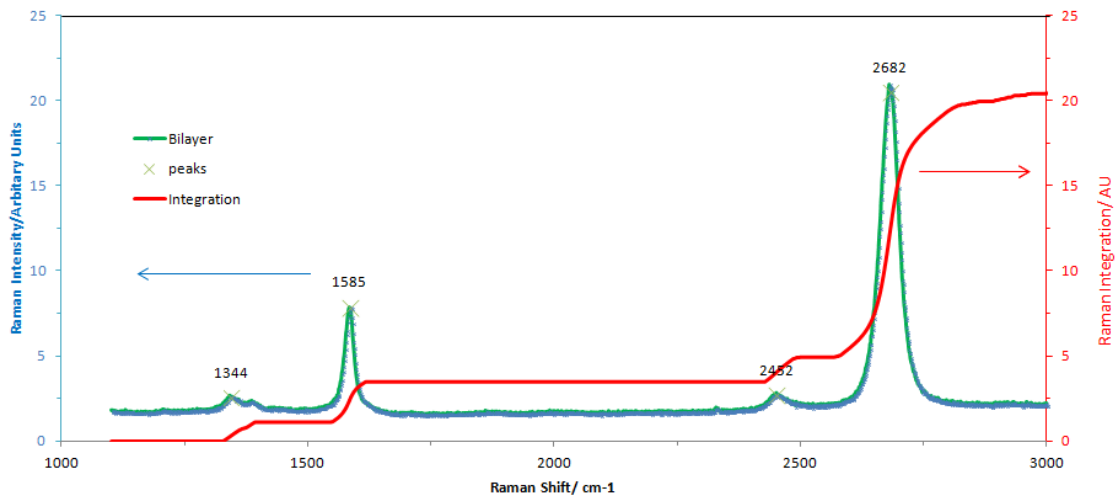


Figure 27. Raman spectrum of Bilayer graphene.

Figure 27 is the Raman spectrum of a bilayer sample of graphene. Optically, sometimes it is hard to distinguish monolayer and bilayer examples; especially difficult if isolated from other "samples" which would allow a side by side comparison. Monolayer and bilayer graphene side by side are comparatively easy to distinguish within an image. The Raman spectrum of bilayer graphene shows a 2D blue shift (ca. 20 wavenumbers), has a FWHM larger than monolayer graphene Raman signal and the peak is definitely split compared to monolayer graphene.

CVD Graphene Raman spectrum with 514 nm excitation

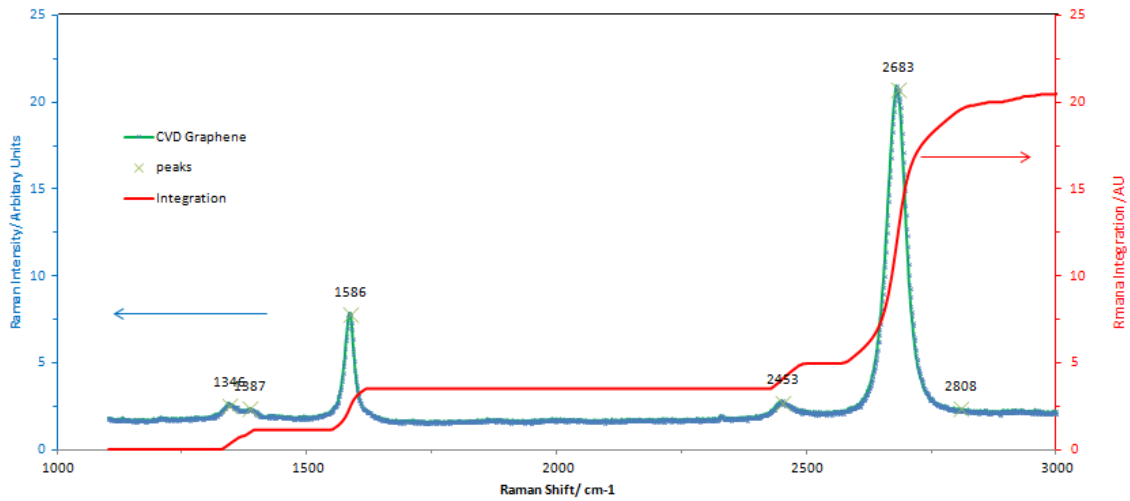


Figure 28. Graphene produced by CVD from methane and hydrogen over copper.

Graphene produced from a CVD process is shown in Figure 28. The 2D peak at 2683 cm^{-1} is very slightly red shifted ($< 3\text{ cm}^{-1}$) and the peak has a FWHM of 56 cm^{-1} . The peak is smoothly increasing, as the first and second derivatives only show one peak turning point. The increased width may be a function of additional impurity from the copper or ferrous ions. The FWHM width of 56 cm^{-1} is approximately double that of single layer graphene but is less than the FWHM of bilayer graphene. The (numerical) integration of the CVD 2D Raman peak is similar to that of monolayer 2D peak, relative to that of the G peak.

2.7 GRAPHENE AND DEFECTS.

Defects are introduced into the graphene structure at numerous points in a fabrication sequence. Some defects might be visible under a high power microscope and be "macroscopic" (rough edges, tears). Other defects might be introduced by lithography or even Raman acquisition. Measurement of the Raman spectrum has lead by Ferreira⁸ to an approximation for the disorder length L_D (nm):

$$\frac{I_D}{I_G} = \frac{C_\lambda}{L_D^2}, \text{ with } C_\lambda \sim 100\text{ nm}^2 \text{ @ } 512\text{ nm}.$$

This empirical relationship is valid up to $\frac{I_D}{I_G} < \sim 3$ giving an area of disorder of approximately 30 nm^2 and a disorder length, L_D , of about 5 nm . Figure 29a shows a damaged graphene sample (deliberate e-

beam exposure) and a plot of measured disorder distance L_D (nm) versus measured Raman spectrum in Figure 29 b. Latter in this work, in order to measure accurate long path lengths to investigate graphene and graphene super lattices $\frac{I_D}{I_G}$ ratios should be as close to 1 as possible for excellent graphene samples.

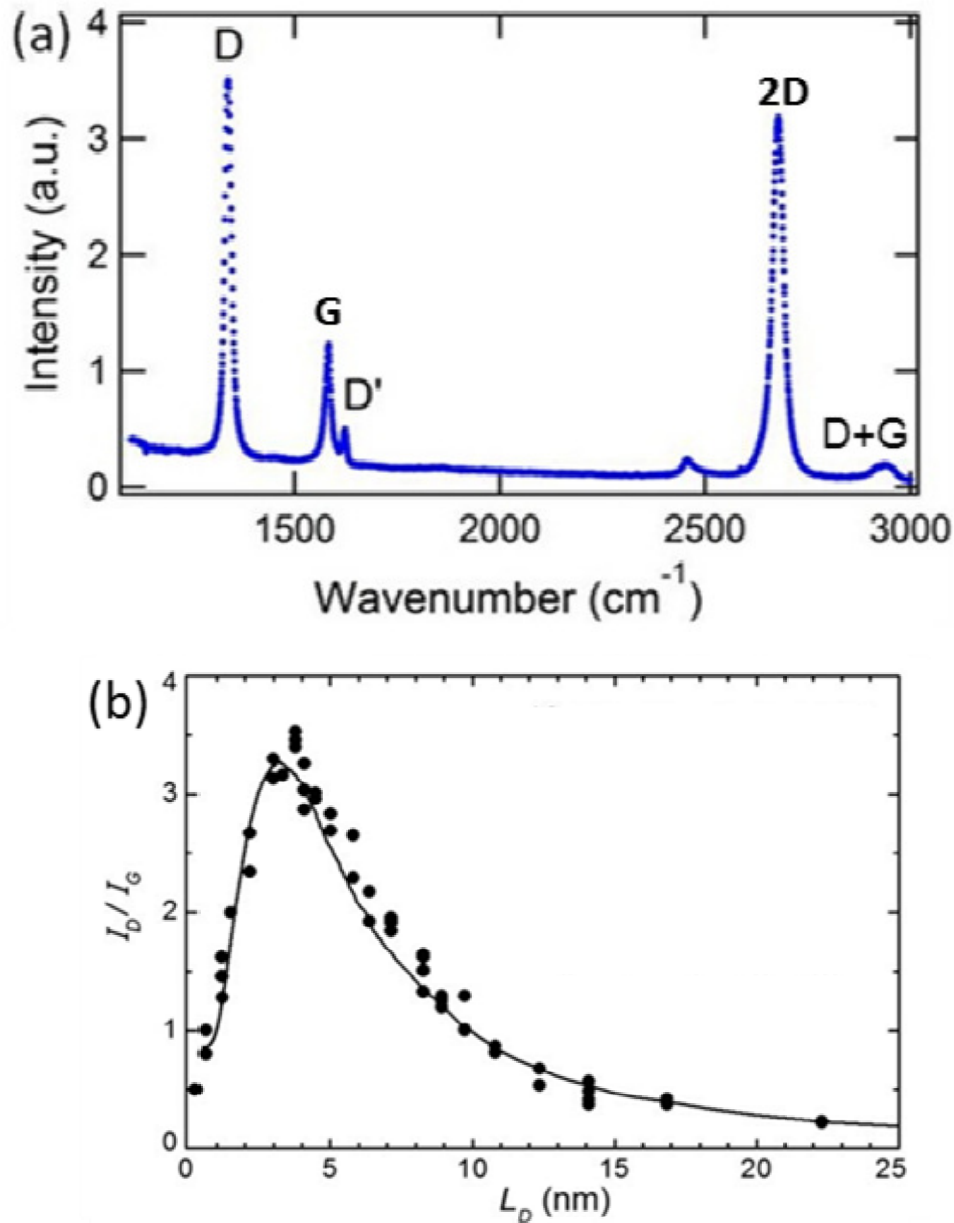


Figure 29. Raman spectrum of graphene irradiated by electron beam, showing significant D, D' and D+G disorder peaks. The concentration of disorder can be extracted from the intensity ratio I_D/I_G . $I_D/I_G \sim 3$ for this spectrum. Figure b shows I_D/I_G as measured to the average distance between defects (L_D) as measured by SEM. Taken from Childres.¹⁹

2.8 References.

1. Y. Aharonov, D. Bohm, *Physical Review*. 1959, 115 (3): 485–491, "Significance of electromagnetic potentials in quantum theory."
2. C.V. Raman, *Indian J. Phys.*, 2 (1928) 387, "A new radiation."
3. J.W. Strutt, (1871). "LVIII. On the scattering of light by small particles." *Philosophical Magazine* **41**(275): 447-454 (Rayleigh).
4. P.A. George, J. Strait, J. Dawlaty, S. Shivaraman, M. Chandrashekha, F. Rana and M.G. Spencer, *Nano Lett.*, 2008, Vol.8, 4248.
5. A. C. Ferrari, J. C. Meyer, V. Scardaci, C. Casiraghi, M. Lazzeri, F. Mauri, S. Piscanec, Da Jiang, K. S. Novoselov, S. Roth, and A. K. Geim. *Phys. Rev. Lett.*, 97:187401, 2006. "Raman spectrum of graphene and graphene layers."
6. V. A. Ermakov, A. V. Alaferdov, A. R. Vaz, E. Perim, Pedro A. S. Autreto, R. Paupitz, D. S. Galvao & S. A. Moshkalev. *Scientific Reports*, 2015, vol. 5, pp. 11546. "Burning Graphene Layer-by-Layer."
7. B. E. A. Saleh, M. C. Teich, *Fundamentals of Photonics*. Wiley Series in Pure and Applied Optics (Wiley, New York, ed. 2, 2007).
8. M.M. Lucchese, F. Stavale, E.H. Ferreira, C. Vilani, M.V.O. Moutinho, R.B. Capaz, C.A. Achete, A. Jorio, *Carbon*, 2010, Vol. 48, pp. 1592-1597
9. I. Childres, L. A. Jauregui, W. Park, et al. Chapter 19, *Raman Spectroscopy of Graphene and Related Materials*. I. Childres, L. A. Jauregui, W. Park, H. Cao and Y. P. Chen. d. J. I. Jang, Nova Science Publishers (2013).
10. A.C. Ferrari, *Solid State Communications*, 143 (2007),pp. 47–57.
11. Y. Miyata, E. Maeda, K. Kamon, R. Kitaura, Y. Sasaki, S. Suzuki, and H. Shinohara, *Applied Physics Express*, 2012, Vol. 5(8), p.85102. "Fabrication and characterization of graphene/hexagonal boron nitride hybrid sheets."

12. M.S. Dresselhaus, A. Jorio, A.G. Souza Filho, and R. Saito, *Philosophical Transactions of the Royal Society A: Mathematical, Physical and Engineering Sciences*, 368(1932), pp.5355-5377. "Defect characterization in graphene and carbon nanotubes using Raman spectroscopy."

CHAPTER 3: EXPERIMENTAL PREPARATION OF GRAPHENE AND GRAPHENE STACKS

Experimental section 1: Fabrication of Devices

This experimental section deals with the processes involved in preparation of graphene fragments and the subsequent processing to either fabricate graphene devices or graphene fragments. The two methods of graphene fabrication are described; one by Chemical Vapour Deposition, and the second by mechanical exfoliation.

3.1 CVD OF GRAPHENE

The work presented in this section was undertaken at the Hong Kong University of Science and Technology due to the safety consideration of handling explosive gases. The author undertook the Chemical Vapour Deposition (CVD) of graphene in order to speed up testing of graphene structures of sufficient size for stacking and electron beam lithography.

Overview.

CVD of graphene is a simple process. A carbon source is atomised over a surface which may act as a catalyst or as a surface to grow the graphene. In these experiments copper was used as a material that has previously been demonstrated to be an effective catalyst for CVD of graphene.¹ After nucleation on the surface in the presence of atomised carbon, graphene "hexagons" grow over the surface. Low nucleation rates give "few hexagons" that can grow as large as 10mm. High nucleation leads to a large number of graphene hexagons which can overlap as they "overgrow" each other or are small, e.g. <1mm. Low growth (low quantity of flow) of methane conditions favour slower growth whilst higher flow rates will tend to favour higher growth rates for the same substrate. In a typical CVD process growth rate of a few 10's of nm per second can lead to large graphene islands of between 300-5 000 micrometers. The graphene islands are then removed from the surface in a similar manner to the mechanical exfoliation route used previously (vide infra).

Experiment: CVD of Graphene growth over copper.⁴

Copper(99.95% pure, 25 micron thick) cleaned pieces were wrapped around a nickel foil (99.95% pure, 25 micron thick) to form an envelope of copper approximately 20 x 10 mm in size. For convenience, the

"top surface" (plain area) of the envelope was taken as the surface of interest and placed facing upward on a quartz pan. The quartz pan was carefully placed half way along a 1 metre quartz tube, of diameter 22 mm, taking care not to scratch the inner surface of the quartz tubing. The quartz pan is centralised in a tube furnace and Argon (99.9% pure) gas was used to flush the tube. Finally, Argon (99.95%) was flowed at 1.00 Standard Cubic Centimetres per Minute (sccm). The tube furnace is ramped to 700 °C (at maximum power the temperature is achieved in 3000 seconds). Argon (99.9%) is introduced at 10.0 sccm and dihydrogen (99.95%) is introduced into the flow. The flow rate of dihydrogen was adjusted to 5.00 sccm using an accurate mass flow meter. The tube furnace is then ramped at 1 °C/10 seconds to a temperature of 1040 °C. The temperature is finally raised to 1048 °C in 100 seconds with a 5.00 sccm dihydrogen flow at atmospheric pressure (not corrected). When the temperature reaches 1048 °C methane gas (99.95%) is introduced at 1.00 sccm with a dihydrogen flow set as previously. The flow is maintained for 600 seconds. After 600 seconds, the power to the tube furnace is set to zero. The gas flows are switched to Argon (10.0 sccm). Once the tube furnace registers 700 °C the tube furnace is removed from the tube/pan (the tube furnace is on a moving rail to facilitate easy location/removal.) The quartz tube and pan was allowed to cool naturally to a point that the tube can be safely handled.

In one embodiment of the process, once the tube reaches approximately 200 °C the tube is connected to a (compressed) air line and the furnace rolled back to the quartz pan with copper substrate; the tube is heated at 200 °C for 600 seconds with air flowing (uncontrolled flow). Copper not covered by the graphene becomes lighter in colour making the graphene islands much easier to see using optical photography and eye.

The tube furnace is removed (rolled away and opened) to allow final cooling of the copper foil.

The graphene carrying copper was removed and the envelope opened; a quick method is to use a pair of scissors to cut the ends to allow the "envelope" to be easily opened with minimum creasing. The nickel foil was discarded and the inner surface of the copper envelope was photographed. The outer part of the envelope was briefly rubbed with extra fine sand paper to remove graphene coverage. Interesting areas of graphene on the inner side of the envelope were selected by cutting the foil carefully around the graphene hexagons with scissors; ensuring that there was "clear" copper around the graphene.

The 1-5 mm "hexagons" of graphene on the copper are spin coated with PMMA (950K, A4, 3000 rpm 60 seconds) to protect the graphene and baked at 150 °C for 3000 seconds. The copper was placed "graphene/PMMA" up on the surface of 1 litre tank of ferric (III) chloride with 0.5% hydrochloric acid.

The surface tension of the solution easily holds the copper on the surface (the PMMA also adds a degree of hydrophobicity helping with floating the copper on the surface of the water.)

The tank was covered to prevent casual contamination of the PMMA and reduced evaporation of the solution at room temperature. After removal of most of the copper (by visual assessment only) the graphene island (copper-graphene-PMMA) was placed on a new solution of ferric (III) chloride with 0.5% hydrochloric acid and left for a further 12-24 hours to remove the copper. Once the island was visually clear of copper, the island (graphene-PMMA) was washed with 0.5% hydrochloric acid (three times) and then five separate distilled water washed. If the solution in the tank tests positive for copper ions (faint green flame or black sulphide paper test) the wash step can be repeated until zero copper detected (less than 1 ppm).

The PMMA membrane was carefully dried on a silicon-silicon dioxide wafer (graphene face down!) by contact transfer and air drying at 80 °C for 1 hour. The silicon-dioxide layer is slightly hydrophobic when clean so aids in the pickup of graphene from the surface. Sometimes, a few drops of IPA in the water (care! well away from graphene membrane!) aids in the quicker transfer of graphene membrane as the surface tension is reduced.

The PMMA membrane was exposed to 360 nm UV radiation (10 watts) for 1000 seconds to partly breakdown the PMMA on the wafer. The wafer was carefully washed with IPA:water 2:1 to leave behind the graphene on the silicon-silicon dioxide.

The graphene was then annealed at 250 °C for 10,000 seconds under argon flow (99%) 1 sccm in a thermal annealer. The graphene can then be treated as per mechanical exfoliation graphene.

3.2 Recrystallisation of hexagonal boron nitride.

Hexagonal boron nitride from two different commercial sources (one labelled MoS₂; a company based in Manchester) and another from China (100 g commercial sample) were ground using nickel balls in a simple ball mill (6 revolutions a second, 20 balls 100% nickel, 0.5 g boron nitride) for 6000 seconds at room temperature.

A portion of the powder and nickel balls (1 mm diameter) were then placed in a graphite crucible and slowly heated to around 1900 K. The nickel melted to form an even (thin) film on the crucible. The temperature was lowered to about 1800 K (+/- 50 K) and left at this temperature for about 3000 seconds before cooling down to 1200 K (1 K/second) then rapidly cooling to ambient at 5 K/second.

Small white crystallites were formed on the nickel surface. The crystals were scrapped off with a sharp knife. If the crystals were well formed (triangular-hexagonal) they were used as is for exfoliation.

Smaller crystals and uneven crystals were mixed with new nickel balls (1 mm diameter) and subject to a second "crystallisation" (same heating profile as previously). The cooled mixture was examined as before. The melted nickel was kept for subsequent re-use as this contained saturated nickel-boron nitride.

Exfoliation of hexagonal-boron nitride.

As previously with graphite, hexagonal-boron nitride (h-BN) crystals were placed on double side tape. One side of the tape was pressed onto a thick glass sheet to give the tape rigidity especially to shear forces. The boron nitride crystals were gently and SLOWLY! pulled apart, with as little shear as possible, about 3 times to generate "small thin fragments". Rapid, and or, multiple tape pulls resulted in many small fragments of less than 5 microns. The tape was then placed on a suitable substrate (silicon-dioxide-290 nm) and gently pressed and slowly removed by pulling at approximately 1mm/ second. Examination under a low power microscope revealed a distribution of crystals in both size and thickness. The largest area and thinnest crystal sections were identified and used in the transfer station to make graphene-boron nitride layers.

h-BN (few layer) crystals are harder to observe than graphene as they have no optical coloured light absorption; graphene absorbs 2% of visible light so can be seen with visible light on a 290 nm silicon dioxide (interference) layer.

3.3 Ultra-Violet Microscopy

In order to better observe h-BN and graphene, a UV microscope was built from a florescence microscope. Graphene and h-BN both have strong UV absorption bands, in the case of graphene these UV absorptions are ten times more intense than the optical (visual) absorption¹ bands as indicated in Figure 30.

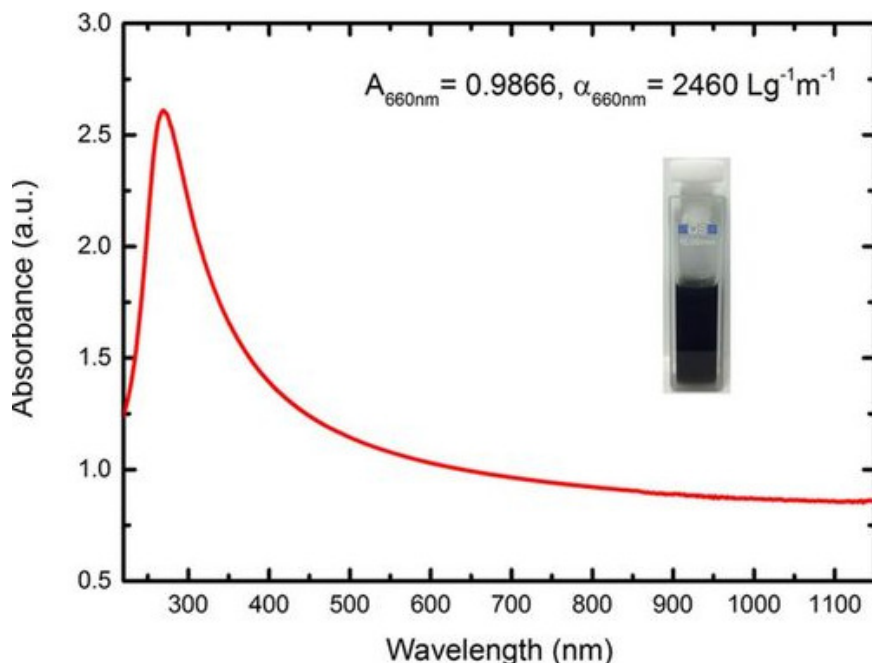


Figure 30. UV-visible-IR spectrum of a graphene solution. A_{660nm} is the adsorption at 660 nm with absorption coefficient α_{660nm} . Taken from Santra.²

A fluorescence microscope uses a UV light source to excite ultra violet absorbers; usually these are fluorophores, in this case the graphene/ h-BN act as (strong) UV absorbers. The reflected light passes through a long pass filter to remove the UV light and let the visible light pass through to the camera or eye piece. The florescence microscope was modified by removing the fluorescence cube; the cube was replaced with "a half silvered mirror;" the UV light can thus be used to illuminate the sample and then is reflected back through the optical assembly to the camera as per Figure 31. As the UV lamp illuminates the sample directly the eyepieces are blanked off for safety and the camera used to record images.

The camera detector was improved dramatically by the following modifications;

1. Removal of IR and anti-moiré filter glasses.
2. Removal of Bayer matrix and optical glass over the sensor sites.

The UV flux from the medium pressure mercury lamp was increased by 75% by removing the filter cubes. The CCD camera detector quantum efficiency (of all light) was increased by 20% by removal of IR and UV filters covering the detector. The main improvement was the use of "half-silvered" mirrors for the light path from the light source to the optical train as mirrors reflect 95-99% of incident light rather than absorption of light in the filter cubes. The direct UV microscope was used to identify graphene and boron nitride materials.

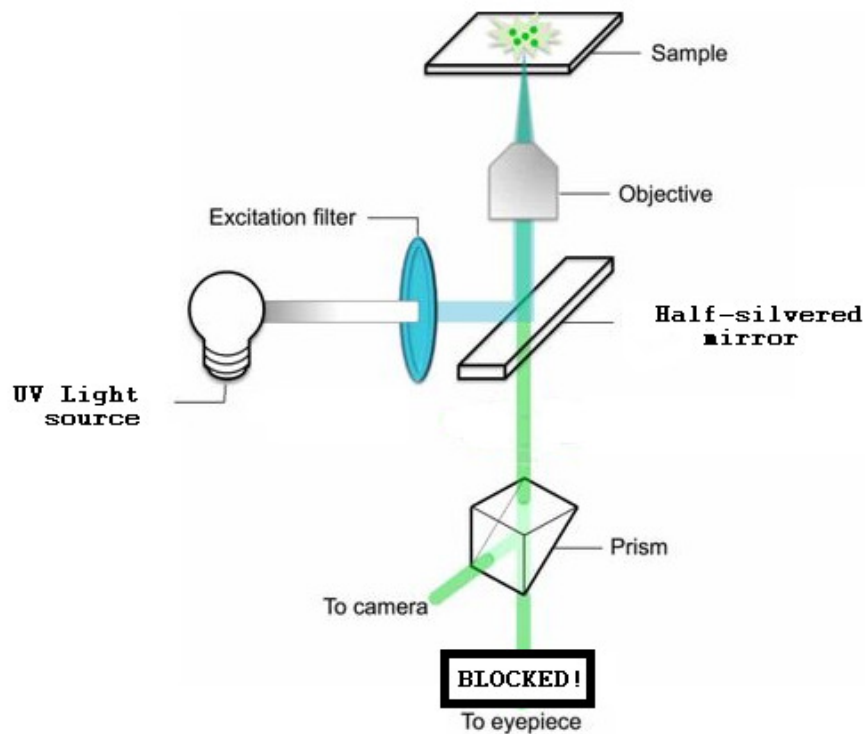


Figure 31. Light path for UV modified microscope. Note, when the UV filter is removed dangerous UV (<360 nm) radiation can pass directly to the eyepiece; hence the eye piece is blocked. The camera used was a normal CCD device capable of detection down to 340 nm.

3.3.1 MANUFACTURE OF 2D GRAPHENE TRANSFER STATION

In order to fabricate graphene-boron nitride “stacked” examples whereby graphene flakes are placed on top of a boron nitride flake an optical transfer station was fabricated. The mechanical considerations for constructing a “stacking station” are:

1. Mechanical stability to within 1 micron (macro vibration free)
2. Optical sight of transfer from layer to layer with:
 - a. Sufficient working distance (around 5 mm) for transfer 2D to 2D.

- b. Sufficient accuracy (around 0.5 microns) for 2D alignment
3. Mobility of the working surfaces in X, Y and Z as well as ideally rotation for accurate placement of layers to be stacked.
4. Temperature control for predictable transfer.

The simplest implementation was to use a pillar microscope with vertical travel of 50 mm together with movement of the whole microscope assembly to cover a 50 mm substrate. The microscope used was a 160mm fixed (interfocal) length focus with three objectives (5, 10 and 20x magnification) Standard 10x and 5 x binocular eye pieces were used. A white light reflecting prism was cemented into the turret to illuminate the substrate area yet allow sight or camera attachment through.

The working distance of the objectives was as per Table 2. An additional 40 x objective with working distance of 5mm was used. As this objective was infinity focus an additional 1-2 mm working distance was achieved with the fixed focus 160mm optical pathway. (See Figure 32).

The base of the microscope was attached to a steel metal plate via a 100 N magnet to allow flexibility of set up and stability of base.

Set up	Working distance /mm	5x eyepiece	10x eyepiece	Camera
5 x objective (160 mm focal length)	10	Scan of surface for suitable pieces	Location of thin pieces(graphene/hBN)	Image 20x20mm
10x objective (160 mm focal length)	3	-	Accurate assessment of 1,2,3 layer graphene	Image of 2D materials and simple x,y measurement
40x LWD (infinity focal length)	~5*	-	Accurate alignment of membrane/substrate	Improved co-linearity of 2D structures.

*Table 2. Transfer station microscope configuration. * 40x objective is infinity objective but used on a 160mm (pre-determined) tube focus microscope: effective working distance ~7 mm with a ca. 35x magnification.*

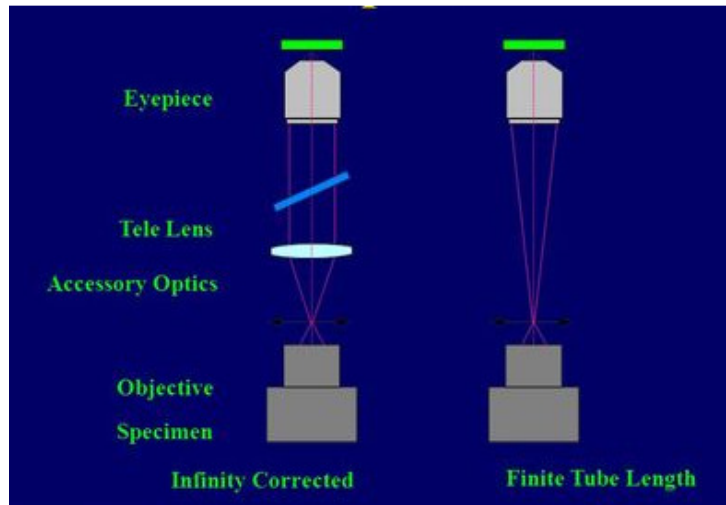


Figure 32. Difference between infinity and 160 (finite) tube objective lens systems. An infinity objective can be used in a finite tube system (but not the other way round).

X, Y, Z and theta table.

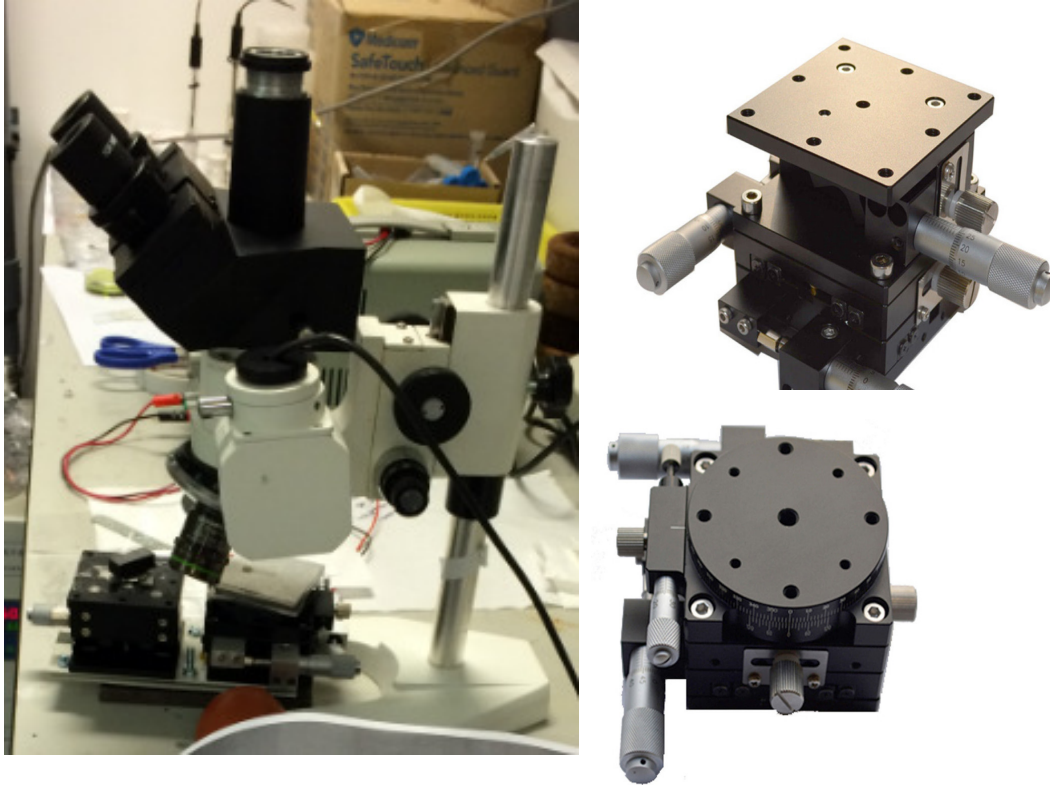


Figure 33. Photograph of stacking "transfer station" with photograph inset of x,y,z control. A rotation stage could be added but reduced working gap and introduced a slight "wobble" in system. In addition a Peltier (heat/cooling) device was added on top of the rotation/Z adjuster.

X, Y, Z optical tables were bolted to a 100 x 100 x 5 mm metal plate for weight and rigidity. Each optical table allowed approximately 5 mm of travel (maximum) whilst the rotation table allowed 360 degrees of rotation. The table was moved manually by micrometre screw gauge. The minimum movement was ca 1 micron and for rotation was ca. 0.3 degree.

A strong rigid glass cantilever arm (3 mm thick) was used to ensure ease of line of sight of substrate at all times. A hole/gap in the cantilever arm of 1 mm was used to act as clear optical pathway for transfer operations from top to bottom. In addition, a Peltier plate was connected to the rotation stage (glued) and a metal "thermal plate" added across the top. The total height of the stack was 35 mm without substrate. The top plate was levelled as much as possible so that the degree of co-planarity was high between the substrate and the transfer arm. Flatness across the substrate was measured by the degree of focus from the pillar microscope. The flatness was measured to within 1 micron across the centre of the x,y,z and theta table.

3.4 EXPERIMENTAL TRANSFER PROCEDURE

A PMMA membrane (A7; 600 nm thick) was cast over 200 nm PVA on a silicon wafer. A circular 5mm diameter score in the PMMA was scratched with a sharp needle. The silicon substrate was carefully slid into a distilled water bath. The PVA dissolved leaving the PMMA to float off onto the water surface. It is very important that water (solution) does not contaminate the top surface: great care is needed to ensure that the PMMA remains fully floating. Surface tension forces help stabilise the floating PMMA. The PMMA membrane was picked up with a smoothed thin washer from underneath still to ensure that the PMMA remains dry. (The washer was thinned and flattened using wet and dry paper to polish the surface to flatness. The pillar microscope was used to determine the mechanical planarity of the washer.)

The ring carrying the membrane was placed on the cantilever arm and glued (10 % PVA/water) in place and gently heated to 100 C for 2000 seconds. The membrane becomes flatter and is stretched; the membrane was checked for optical clarity (voids, bubbles or tears) using the pillar microscope. A good membrane is deemed to be formed when the membrane was uniform and was optically clear. Due to surface imperfections (micro-bubbles/particles) it is possible to measure membrane thickness using the pillar microscope and focus point.

A substrate was placed on the transfer table; for convenience this was glued in place using 10% PVA glue. A h-BN flake of sufficient size (> 40 micron) and thinness was centred on the transfer table after examination by the pillar microscope at low power (10x magnification). The ring carrying the membrane was centred over the h-BN flake. Looking through the gap in the cantilever arm and the ring itself, the supported membrane of PMMA was lowered onto the BN flake. If the system is co-linear and flat parts of the membrane may come into contact with the substrate or flake. Several attempts maybe needed to ensure the membrane fully covers and attached itself to the target BN flake. Using the heating Peltier the temperature of the substrate was raised to around 50-60C. The membrane can be "pressed" onto the surface with the aid of an air cannon. As the membrane sticks to the flake it can be observed to alter optical characteristics. The different optical densities produce a change in optical characteristic that can be easily observed through the eye piece. Once the PMMA membrane is covering the BN flake the mechanical arm can be slowly raised (~1 micron per minute). The microscope can be used to verify that the membrane is removing the BN flake from the substrate as the arm/ring/membrane is raised up and the BN flake is lifted off. The flake can then be removed from the substrate.

A graphene/graphite substrate was prepared. The surface was annealed at 600 K in 10% hydrogen for 4000 seconds. A clean graphene flake was centred on the stage and the previously attached BN flake roughly aligned by 5x magnification objective. When the h-BN flake on the membrane was approximately a few microns above the graphene a 50x objective was used to carefully align the two flakes using the eye piece cross marker.

The h-BN flake bearing membrane was carefully lowered making corrections in pathway as the membrane was lowered at about 25 nm/second. Once the membrane and BN flake had touched the graphene the substrate was warmed to 60-80 C to aid the membrane to contact the lower substrate containing the graphene. The heating of the substrate was continued until the membrane bearing the flake fully contacts the graphene; again observable by optical means as the refractive index changes on contact. The system was annealed for around 1000 seconds to allow the BN to fully contact the graphene. The top membrane can be pulled away (very slowly!) at about 50 nm/second. Around 10% of operations results in successful pick up of graphene from the substrate to the BN fragment. If unsuccessful, the membrane can be lowered again and the processes repeated. As the membrane has already made contact with the substrate the n^{th} touchdown was usually faster than the first or previous example. Around 25% of touchdown/lift off of the membrane result in macro tears (visible to the eye) whilst around 5% of movements of the membrane result in serious tears (around 50 microns or bigger). At the second, or n^{th} touch down the temperature was raised by about 10 C to help membrane “mould” to the graphene. As the temperature approaches 100 C the membrane becomes very pliable and weak due to the approach of the glass transition temperature of the polymer.

Once, the graphene has been removed from the substrate, the graphene (graphene-BN-membrane) was carried to another h-BN flake, ideally slightly larger than the original BN flake to form a Si-SiO₂-h-BN-Graphene-h-BN –membrane layer structure. The final removal of the membrane was extremely difficult and was only achieved in around 5% of cases. The simplest procedure was to heat the membrane to ca 120 to effectively melt the membrane to the substrate. Air cannon can be used to ensure a clean tear of the membrane from the carrier (a hair drier is very effective). The remaining membrane can be gently washed (care!) with acetone and then cleaned in a reducing atmosphere at 300 C.

3.5 LITHOGRAPHY TO FABRICATE DEVICES.

In order to generate a device for testing electron mobility (resistance) the graphene (and h-BN) pieces have irregular shape and size. This section deals with fabrication of a working device using lithography. Lithography is a standard technique for micron and nano device fabrication.

A h-BN-graphene-h-BN stack of approximate > 100nm thick is not suitable for fine scale E-Beam lithography; hence only thinnest h-BN flakes were used. A7 or even A11 PMMA was spun on the substrate to form a 500 nm thick resist layer. (3000 RPM for 60 seconds) followed by baking at 120 for 1000 seconds and then ramped up to 180 C for 3000 seconds.

Large scale structures (pads, tracks and marks) are drawn on the resist using low resolution settings:

1. 1000 micron field settings
2. 1-3 nA current
3. 400 uC resist dosing
4. Alignment by positioning (min/max top bottom/left right)
5. Second (large) aperture for approximate 20 nm beam size.

For low resolution work calibration is not strictly necessary. However, focus and measurement of beam current are both vital and essential for future processing steps. Location of substrate by SEM measurement is accurate to around 500 nm and this is sufficient for early stage lithography work. An alignment pattern (see Figure 33) is also drawn so that future alignment is faster and reliable. Such a pattern is based upon design in AutoCAD. A typical lithography exposure of 1000 seconds is sufficient for low resolution work.

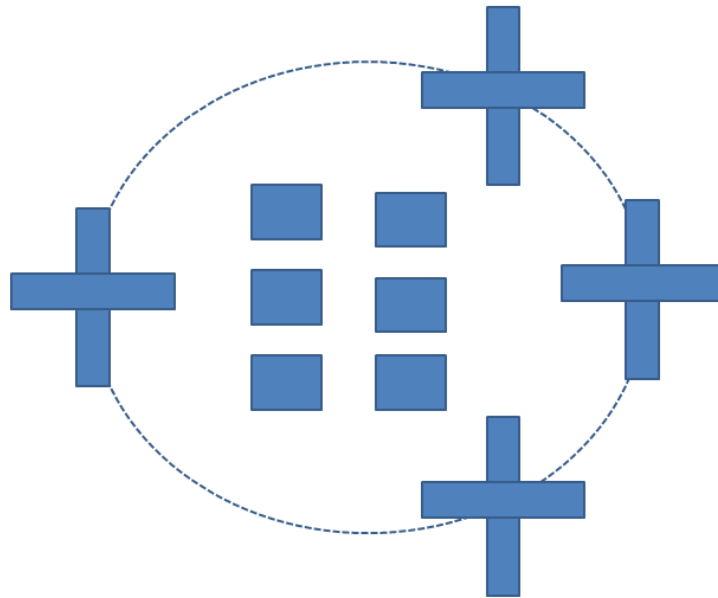


Figure 34. Schematic of AutoCAD alignment and pad Ebeam lithography for low resolution writing, prepping for fine scale write of graphene near pads

Development system.

Development is tested in-situ by measuring removal of resist with optical microscopy. Phase contrast or dark field microscopy is especially useful to determine the absence of resist in the channels/structures exposure, whether by Ebeam or photolithography. The following recipe was used for positive resist of PMMA: exposure results in species that are reduced in molecular mass and (far) more soluble in the developer.

1. 2:1 IPA:water (at 20 C) premixed for 5 minutes was used as developer
2. Development of resist for 55 seconds followed by quench 1:99 IPA:water .
3. Observation of pattern clearing. (using microscope)
4. Fresh (!important!) 2:1 IPA:water for further development from 10 to 100% of time of previous development depending upon structure size.
5. Quench 1:99 ipa:water
6. Photograph substrate and store data for reference.
7. Oxygen plasma clean substrate (5-30 W power, 500 micro-torr pressure) 20 seconds
8. 15 minute exposure in UV 15 W flood bank to reduce lift off time further.

The substrate is then ready for metallisation.

IPA (100%) can be used on its own for very slow resist removal and 3:1 IPA:water results in times that are approximately 4 x longer. Definition of edges is reduced with slower developers.

Metallisation.

Titanium-gold baskets are warmed to 95% of evaporation temperature inside an oven at $10^{\text{exp}-2}$ Pascal or better. Out gassing was observed in all cases. It is important to pre-outgas both metal samples as this gas can seriously reduce purity at the interface of the titanium-gold; poor interfaces results in failure of metal to stick to substrate. In this work substrate-gold (titanium) failure rates were high, approximately 20%. Other systems such as chromium, aluminium (alone, no interface needed) and niobium gave excellent wafer - metal adhesion without the need for an intermediate layer.

Sequentially, metals are evaporated at 100-110% of evaporation temperatures (power). Target deposition rates of at least 0.1 nm/second are sought. Maximum deposition rates of around 10 nm/second or greater are difficult to control and measure and so are avoided where possible.

Initially, Titanium 2-8 nm was deposited followed by Gold (10-20 x titanium layer thickness) as quickly as possible thereafter to increase titanium-gold adhesion properties.

Metal lift off

During metallisation, the whole surface is deposited with the target metal source. In some cases areas can be "screened off" with an organic (tape) or hard (glass/metal) mask. The unscreened areas contain "exposed and developed" lithographic pattern plus the resist mask covering. The excess lithographic resist mask was removed with solubilising agent of acetone. The acetone can be gently warmed (ca 300 K) and gently agitated. After around 10,000 seconds some of the excess metal should be able to be seen to be lifting off. Further agitation may be useful. New solvent was introduced every 10,000 seconds to help clean the excess metal. If after around 100,000 seconds progress was slow/incomplete a 3 second burst of 50 % Ultrasound (approximately 50 W) can be used to accelerate the metal removal. Further 3-10 second ultra sound energy agitations are performed with careful investigation using 10 x optical microscopy to assess damage to the metal structure.

After approximately 30 seconds of ultra sound energy agitation damage to metal surfaces in all areas begins to be observed. However, graphene fragments survive 100 seconds, or longer, of high energy ultrasound (100 W or more). (Test pieces of graphene were used to calibrate and check ultra sound damage).

Further metal lift off with the help of directed solvent jetting can be useful. Graphene has been shown to be sufficiently bonded to substrates to with-stand 60 seconds of hand jetting of acetone.

Fine scale lithography.

Once there is sufficient accurate high definition location marks on the substrate surface within a reasonable distance of the target flake (less than 100 microns), ideally less than 50 microns from the target flake, then electron beam machining of connects and Hall bar formation are possible. The field width for the ebeam is 100 microns; movement or measurement outside of this range involves movement of the cassette carrying the sample. Accurate photomicrographs of the flake and calibration marks at 2x, 5x and 10x are digitally combined to build a montage picture. The montage picture is then used within a software package for drawing Hall bar and filigree connectors from contact pads to the target flake.

The three most important experimental considerations are:

1. Accurate distance measurements of calibration marks
2. Accurate angle estimations of calibration marks
3. Excellent definition of calibration marks (straight walls)

The registration (calibration) marks are measured a minimum of three times or to a repeatability of less than 200 nm. Settling time of the system can be 600-3000 seconds and mainly can be monitored by the temperature of the carriage and repeating calibration measurements. When (set) calibration measurements vary less than ca. 20 nm this is a reasonable estimation of machine stability.

The registration mark locations are transferred to the AutoCAD file and the AutoCAD file is “calibrated” to these measurements. The correct exposure pattern then determined around some basic rules:

1. Minimum line widths of 2 microns.
2. Closest approach of two adjacent “tracks” 2.5 microns
3. “Tracks” to avoid significant debris / faults on substrate.
4. Accurate scale, rotation and orientation to be checked.
5. Transfer of final drawing completed from new AutoCAD file to eliminate software transfer errors.

Validation of the drawing file and entry of coordinates of the registration marks can be completed. The final current measurement and (automatic) registration pre-write check does not use the same method as the calibration part so further (small) errors can be introduced at this point. For security of write

operations the registration check is done by “manual find” so that better consistency of write calibration is achieved. Differences of up to 500 nm have been noted between the two methods of calibration.

Fine scale work system settings are:

1. Current of maximum 300pA (beam width <20 nm)
2. Accurate focus and astigmatism
3. Single field size for exposure
4. Shot setting of 2 maximum

Development of fine scale work is done in three steps using 2:1 IPA/water with 45 seconds development, check, new solution 10 seconds 2:1 IPA, check, and finally 5-15 seconds 2:1 IPA/water. A final 12 second oxygen plasma with 15W power 500mT is undertaken to give final clean substrate.

Optical lithography.

Once a piece of graphene, whether mechanically exfoliated or grown by CVD, is reasonably characterised, by optical density, Raman or AFM efficient device fabrication is essential. The first task is to identify where on a suitable surface the graphene piece is located, requiring location and orientation to be precisely defined. Optically characterisation of the microscope system (lens, focus and camera) leads to a "flat field" approximation so that angles and distances on a flat surface can be measured. Accuracy of 10 microns is achievable with wide field (low magnification) microscope lens/camera suitable for starting device fabrication.

Positive lithography.

Graphene has been shown to be sensitive to laser, UV and electron beams energy sources. For the measurements of mobility in graphene, as few crystal lattice defects as possible should be introduced by device fabrication. Therefore, positive (processing) resists for device fabrication are to be greatly preferred. Positive processing allows energy sources to not be directed at graphene structures of interest.

Graphene mobility is sensitive to doping. Visible light lithography through a mask, as per Figure 35, results in acid, dye and some solvent doping of graphene. PMMA used in this work is initially dissolved in anisole at 11% concentration. PMMA and anisole interact only weakly with graphene and PMMA is easy to remove with acetone and even IPA:water (ratio greater 1:1).

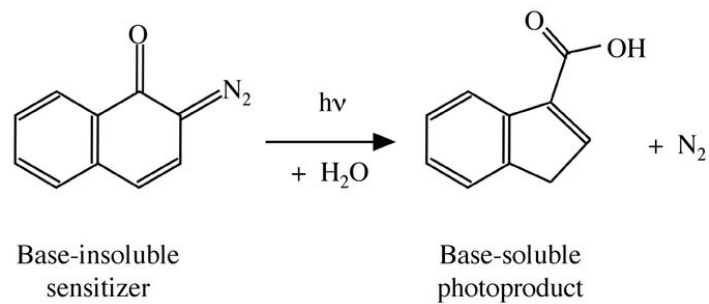


Figure 35. Dye exposure results in photochemical reaction; a chemical rearrangement resulting in an acid salt; the acid salt is solubilised by the TetraEthly Ammonium Hydroxide (TEAH) in water and hence is a "positive resist."

The PMMA requires UV radiation ($200 < \lambda < 350$ nm) which has minimal, or no effect, on graphene doping and stability. Use of PMMA for (optical) lithography for marking (cross and latter dot) for accurate alignment and mapping with calibration is useful for avoiding doping.

Optical lithography allows around 500 nm resolution which can then be used for registration of E-beam lithography. The Jeol EB 6700 system used in this work has a working resolution of 5 nm with a registration accuracy of 10-20 nm (within field) and around 100nm between fields.

In order to minimise doping of graphene structures, the minimum number of steps of lithography is desirable. The following is an ideal minimum number of steps:

1. Registration marks and simple macro patterns (conduction tracks and pads)
2. Fine scale registration and adjacent to graphene patterning
3. Hall bar interconnects accurate to 100 nm
4. Hall Bar design etching of graphene accurate to ca 50 nm

Most lithography steps have a "plasma" cleaning step either pre-metallisation or indeed, for the actual etching. Plasma can attack graphene very quickly (see below) and hence planning the exposure program is vital.

Effects of Plasma on Graphene

Plasma processing involves the following physical conditions: controlled pressure, controlled temperature, controlled (electromagnetic) radio power, control gas composition and ideally constant geometrical confinement with controlled timing.

Graphene is strongly sensitive to plasma processing due to:

1. High electric fields (graphene is an excellent conductor) causing voltage breakdown or excess current in graphene fragment.
2. Oxygen or reactive species readily form graphene-oxide, or graphene lattice defects

In this work, constant geometry or controlled geometry, was rarely achieved as graphene was "randomly" produced and silicon pieces were similar but never identical in shape and size. Most recipes used in this work were generic plasma cleaning or plasma processing recipes modified for the sample presented, or plasma processing was conducted step wise: processing effects measured over predetermined time interval until processing was measured as complete.

Process Stability

The process of generating graphene from graphite involves around 30 clean room procedural steps. In this section process stability will be discussed with estimates of process success.

Step 1. Graphite preparation

Graphite is a mineral and different mining sources have different properties (composition, purity) and crystal properties. Sources used in this study were used as received and appeared to be clean. Larger pieces were split manually by hand so that pieces were around 500 microns or less. Salt, sodium chloride, was found occasional in larger pieces as well as calcium carbonate. Pieces of split graphite were observed under low power light to check homogeneity and lustre. Pieces or poor lustre or homogeneity were not used.

Step 2. Graphite exfoliation

The specific target is to generate a large, bigger than 10 x 10 micron, single layer piece of graphene from the graphite. Graphene is obtained when a single layer from another fragment of graphite. This exfoliation event can happen at any stage of "exfoliation". Each exfoliation event, splitting using the scotch tape method, causes crystal defects along the planes and splitting of crystals. A typical sample of graphite might contain triangular crystallites of ca 1mm; a typical peel, or exfoliation event, will reduce the area of these domains by a factor of 4.

Introduction of shear when peeling graphite causes extensive crystal damage and rapid reduction of crystallite sizes. Application of a device to limit shear during peeling (apart of graphite and laying down to substrate) increases the chance of larg(er) graphene fragments. Zheng⁴ found the shear strength of graphite to much smaller (0.1 MPa) than previously measured. Shear introduces tears, curved edges, defects and "rolling" of edges on the graphene.

Whilst most types of tape produce "exfoliation" that is will cause interlayer splitting, the nature of the tape for the final deposition to a substrate, such as on to silicon-silicon dioxide, is very important. Apparently similar tapes result in variation of deposition ratios. For example, water soluble (CM grade) blue electrostatic tape results in 10-40% transfer of flakes to silicon-silicon dioxide, whilst medium tack blue tape results in 1-2 % transfer of flakes to the same substrate. Indeed, the medium tack tape can reduce flakes on a substrate from 40% coverage to effectively zero. i.e. the tape can be used to remove (multi)graphene fragments.

Step 3. Rapid identification of graphene

Single layer graphene from exfoliation is produced randomly, sometimes no single layer flakes are observed. If there is a considerable amount of graphite debris on the substrate, the time required to search a substrate can be considerable. A simple IPA rinse or an IPA low power ultrasound clean (10 Watts, 10 seconds) is sufficient to remove large graphite debris and allow faster searching for graphene fragments. The IPA clean also benefits the removal of some glue residues. Large amounts of glue from the tape on the substrate can be partially removed with IPA, then water, then IPA rinse. Previous tests had shown that water or IPA ultra sound clean at low power (<50 Watts for 30 seconds) does not remove graphene from the substrate.

Graphene absorbs around 2% of incident light across the visible and IR (> 1000 nm) and considerably higher adsorption at <300 nm. Multi layers of graphene absorb more light and have greater "edge" effects under dark field illumination. Camera luminance measurement (spot or line) can infer approximate absorption for a region of interest.

If a single-layer graphene fragment is observed a high magnification image is recorded together with long exposure dark field illumination. Dark field illumination identifies "dirt" or residues (especially glue) under/on the graphene.

If the graphene fragment appears free from defect or excessive dirt and is a reasonable shape and size further details of the sample can be recorded.

Step 4. Annealing

Once a graphene fragment has been identified, as above, the sample is annealed to remove surface contamination such as glue from the transfer process. Trapped species (mainly water) between the substrate and graphene are also removed, albeit more slowly, by annealing the sample.

Annealing in the Lancaster clean rooms used one of two processes:

1. High vacuum (0.1-10 Pa) annealing at 600K for ca 2 hours, or
2. Annealing in inert dinitrogen/argon, or dihydrogen gas at normal pressure, at 600K for 1-2 hours.

The second process appeared to give cleaner graphene fragments, as recorded by dark field illumination, for glue removal. Dark field microscopy is an ideal tool for detection of edges as shadows are created with high contrast.

Annealing improves probability of success for latter stages. However, as another processing step annealing causes approximately 5% failure (of total process) due to losses of graphene fragments; the losses probably result from large "forces" caused by volatilisation of contaminants (water, solvent) underneath the graphene and thermal stresses.

The annealing process results in substrate and graphene fragment suitable for further processing. Wherever possible, the graphene flake was measured by Raman at this point to determine number of layers and likely purity.

Once a graphene fragment has been identified, analysed and isolated, either by membrane transfer or CVD "float" the flake can be processed by lithography to make devices for I-V measurement.

3.6 MULTILAYER 2D STACKING FOR SUPER LATTICES.

Superlattices as discussed previously are a combination of two similar crystal systems that results in a new crystal system that corresponds to a Moiré pattern found from the two original crystal patterns.

Two different superlattice systems were attempted:

1. Graphene-graphene superlattice
2. Graphene-BN (aligned) superlattice

Each will be described experimentally.

1. Graphene = Graphene bilayer

Copper foil (99.9%, 25 micron) was cleaned by dipping in sulphuric acid (1 molal) for 10 seconds followed by three dips in distilled water. The copper foil was carefully folded around a nickel foam mesh to form a 30x20x5 mm copper jacket. The composite material was placed on a 40 mm quartz boat and then set in a 50mm quartz tube (around 1 m long). The tube was placed approximately centrally in a split tube furnace on wheels.

The furnace was warmed to 600 °C for 1000 seconds with hydrogen flow rate of 1.00 cm³/s flow to dry the copper and quartz parts. Methane (99.99 %) and hydrogen (99.99 %) flow rates of 2.00 and 18.0 cm³/s respectively were introduced and the split oven taken up to 1048 °C as fast as possible (around 2000 seconds). The temperature was maintained as this for 3600 seconds. The furnace was then switched off and rolled upstream for the tube and copper to cool quickly (ca. 2000 seconds). The gas flow was reduced slowly to zero.

The copper foil was carefully “cut open” the inside surface was placed down wards on a 200 °C open hotplate for 1000 seconds to oxidise. Graphene areas were clearly visible as “bright” copper on a dark oxidised plate.

On cooling, PMMA was spin coated and the copper floated on an iron sulphate (saturated) solution (1 % sulphuric acid) for 12 hours. The solution was refreshed and copper removed over the next 12-24 hours. Once the PMMA film was clear to the eye the film was washed in purified water.

The 1-3 mm hexagonal graphene fragments where then placed on silicon-silicon oxide (300 nm) wafers and treated as previously for exfoliated graphene.

A second graphene “layer” was kept on the PMMA film and attached to the transfer station.

2. Graphene-boron nitride bilayer

Using a normal microscope a piece of thin hexagonal-boron nitride on a silicon dioxide-silicon wafer was identified using the following criteria:

1. A thin piece with colour yellow or pink but definitely not blue.

2. Of size of at least 50 micrometers in one dimension and ideally greater than 20 micrometers in second dimension
3. Away from the edge of substrate (> 100 microns ideally) or large pieces/debris of h-boron nitride
4. having a large flat "plateaux" of one colour (uniform thickness)

Typically, after carefully exfoliation of h-boron nitride approximately 1:500 pieces might meet such a requirement.

As per 1 above a "graphene" fragment (clearly identified as 1 atom thick) was found on a separate wafer. Using the transfer microscope, a PMMA membrane was used to lift the graphene fragment from its wafer. The graphene and PMMA were dried in vacuo (1 Pascal) at room temperature for 1-2 hours to remove macro water/solvent contamination. The PMMA membrane was then set up so that a clear optical path for a LWD microscope objective could be used to co-align the graphene and h-boron nitride samples. Carefully lowering the graphene onto the h-boron nitride at a rate of ca. 1 micrometer/minute the graphene was allowed to come into contact with the h-boron nitride. Carefully warming the system to about 80 C allowed the membrane to be lifted off from the substrate; sometimes 3-5 attempts were needed to "release" the graphene from the PMMA to the h-boron nitride. The temperature was raised by 5 °C at each attempt (temperatures >100 °C are problematic to control and allow the PMMA membrane to remain intact.) Attempts to "release" the graphene from the membrane onto the h-boron nitride without a change in temperature always resulted in failure. (no transfer of graphene).

If temperature / number of attempts became impractical it was possible to destroy the membrane and let the graphene "fall" onto the h-boron nitride. In nearly all cases, bar one, the graphene failed to lie flat on the boron nitride and hence the fabrication failed.

3.7 REFERENCES.

1. B. Hu, Z. Wei, H. Ago, Y. Jin, M. Xia, Z. Luo, & Y. Liu, . *Science China Chemistry*, 2014, Vol. 57(6), 895-901. "Effects of substrate and transfer on CVD-grown graphene over sapphire-induced Cu films."
2. K.F. Mak, L. Ju, F. Wang, and T.F. Heinz. *Solid State Communications*, 2012, Vol. 152(15), pp.1341-1349. "Optical spectroscopy of graphene: From the far infrared to the ultraviolet."
3. S. Santra, G. Hu, R.C.T. Howe, A. De Luca, S.Z. Ali, F. Udrea, J.W. Gardner, S.K. Ray, P.K. Guha, T. Hasan, *Scientific Reports*, 2015, Vol. 5, P. 17374, "CMOS integration of inkjet-printed graphene for humidity sensing."
4. R. He, L. Zhao, N. Petrone, K.S. Kim, M. Roth, J. Hone, P. Kim, A. Pasupathy, and A. Pinczuk, *Nano letters*, 2012, 12(5), pp.2408-2413. "Large physisorption strain in chemical vapor deposition of graphene on copper substrates."

CHAPTER 4. MEASUREMENT OF ELECTRICAL AND MAGNETIC PROPERTIES OF GRAPHENE

The accurate measurement of I-V curves for a graphene device of known dimension, width and length can lead to accurate measurement of the mobility of charge carriers. This follows from Drude's law and Ohm's law as previously explored. The number of charge carriers can be accessed from Hall measurements. Furthermore, with controlled external temperature and magnetic conditions, quantum properties of the system can be explored. The use of magnetic fields allows the measurement of Landau levels.

This chapter describes the experimental set-up for measuring graphene devices fabricated in the clean room.

4.1 CONNECTOR FOR GRAPHENE MEASUREMENT

The e-beam lithography described previously generates conducting pathways made of gold (or as described; niobium or aluminium). The lithography generates pads 0.15×0.15 mm separated by 0.2 mm on a substrate of ca 5×5 mm. The connections on the substrate need to be addressed in a systematic manner to allow multiple measurements and tests to be conducted on the graphene device with voltage and current meters.

In the clean room the substrate can be glued to an Leadless Chip Carrier such as that in Figure 26.

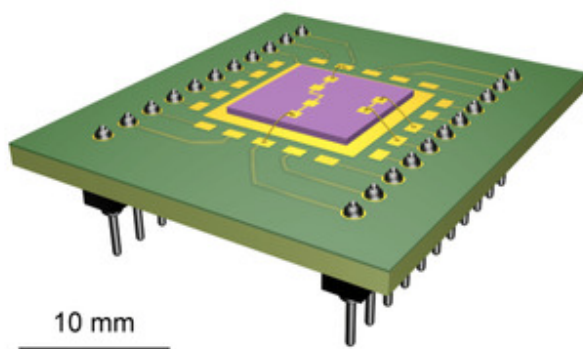


Figure 36a. Graphene-silicon wire bonded to ceramic carrier.

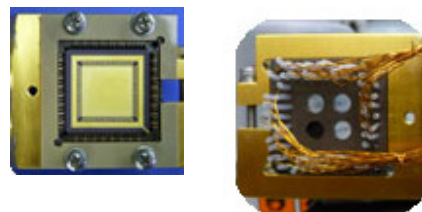


Figure 36b. Picture of head of probe for accepting carrier.

The graphene device and substrate are glued, to the LCC to ensure a robust system and that the graphene, and substrate, is horizontal, important for the direction of the magnetic field and measurement of the Hall effect.. The contacts of the LCC are matched with a J type ceramic acceptor so that the graphene device can then be connected to non-magnetic wires via a suitable connector. In the case of the equipment used for these experiments, the device is placed on the end of a ca. 2.0 m lance carrying the wires away from the LCC to external equipment. The lance allows the graphene device and chip carrier to be lowered into a superconducting magnet and placed inside the cryostat containing the liquid helium.

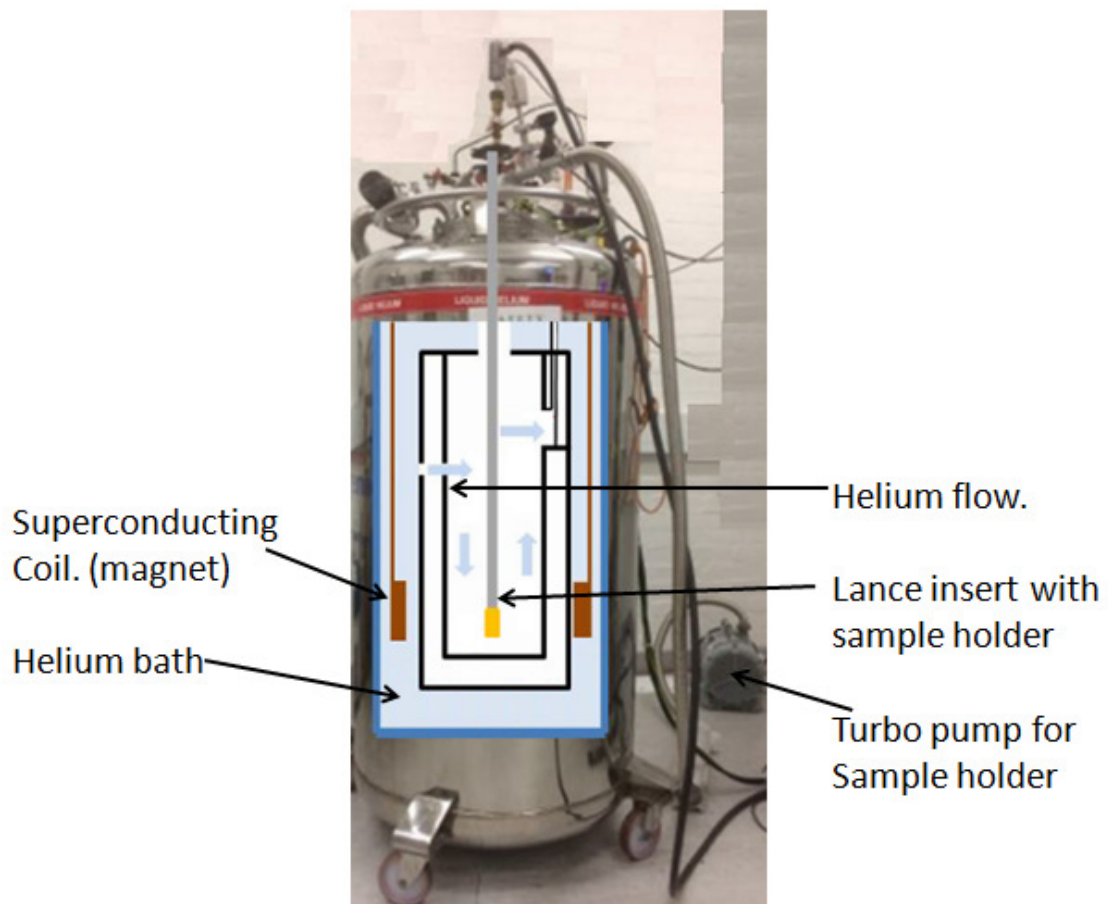


Figure 37. Schematic diagram of structure of cryostat for I-V measurement of graphene samples. The safety features such as valves and vents are not shown. The main Dewar is doubled skinned and made of non-magnetic steel and grounded.

The chip carrier and J acceptor are made of ceramic to ensure a low temperature coefficient of expansion. This prevents unnecessary strain on the J connectors or twisting forces on the silicon-silicon dioxide substrate. To protect the graphene device and the LCC a brass metal cover, is placed over the end of the lance to aid temperature control of the chip itself. However, the metal cover represents a large thermal mass; much higher than the graphene and substrate, in effect slowing cooling and acting as a thermal buffer; ie rapid thermal variations are avoided when changing helium flow in the cryostat. The chip carrier is connected to a gas line so that the space around the substrate can be evacuated. This prevents water and carbon dioxide ices forming as well as liquid dioxygen formation when cooled to e.g. 4 K. It is convenient to evacuate the sample space using a turbo pump for 1-3 hours at 10^{-3} Pa. This helps removes incidental contamination such as water vapour from the surfaces of the whole system and in addition helps eliminate adsorb materials from the graphene surface.

The liquid helium tank is vacuum insulated, and acts as a heat sink reservoir for the sample. Gas can "leak" out of the helium reservoir through a needle valve. The helium vapour then acts as a refrigerant to the (metal) chip carrier. Pumping the helium gas away increases the heat removal and can lower the helium vapour pressure and temperature around the chip carrier. Hence, the chip can be cooled, by gas flow refrigeration, to below 4.2K. Restricting the flow of helium and activating a (low wattage) heater can be used to "set" the temperature of the chip carrier as required.

The superconducting magnetic coils sit in the liquid helium bath. The total volume of the liquid helium bath is ca. 140 litres with reservoir of ca. 50 litres required for the continued operation of the superconducting magnet. With a helium boil off rate of ca, 0.5 l per hour a fully charged liquid helium cryostat can be operated for about 4 days before a refill is necessary. Variations in heating, cooling and the magnetic field required can alter this duration. A superconducting wire sensor is used to measure the liquid helium depth, the length of wire above the liquid helium has a well known resistance (from Ohm's law) whilst the wire in the liquid helium is superconducting, and in effect, has zero resistance. Hence, the helium level can be monitored via a simple resistance measurement of the superconducting wire. It is desirable that the magnetic coil is at the superconductor temperature at all times. This reduces mechanical (thermal strain) and there is less chance of an uncontrolled quench.

When a current is applied in the superconducting coil, the magnetic field generated is perpendicular to the chip carrier, that is, vertically. Hence, this geometry allows measurements to be made of the Hall effect. As the electromagnet has super conductor wires the general equation applies. The wires are thin and can carry high current giving high magnetic fields:

$$B_z = \mu_0 n I$$

Where B_z is the field strength in Tesla, I is the current, n is the number of turns (per meter) and μ is the magnetic permeability (assumed to be μ_0). In the Oxford instruments magnet, the wires are 100 microns width and carry a current of ca. 100 amps. This gives a B_z of (approximately) 15 Tesla. Normal (copper) wires of 100 microns would be able to support 0.5 amps and so the maximum B_z would be ca. 1 T. The superconductor wire used consists of a copper wire with the superconductor material embed inside: the copper acts a support against Lorentz forces and as thermal barrier. The current in the copper wire can be safely ignored, with the copper acting as a insulator around the superconducting wires. The electro magnet coil does not have any shim coils so the field is assumed to be uniform. In the centre of the electromagnet the field should be uniform: ensuring the measurement is made consistently in the same region (repetition of measurements) then the field should be stable and consistent. Indeed, if a set of measurements can be made without withdrawing the sample then that measurement for the sample will be consistent.

The sample is placed as near the centre of the solenoid in order that the magnetic field is as uniform as possible. The total depth of the system to the centre of the solenoid coil through the cryostat and valves is ca. 2 m.

Temperature control of the LCC and graphene.

If the graphene is placed in the cryostat directly, the sample would (eventually) reach equilibrium temperature with the helium bath and attain 4K via conduction and radiative loss. The variable temperature insertion lance is thermally isolated from the cryostat with a space that can be pumped. This space is pumped to ensure that condensates do not form (water, carbon dioxide). Furthermore, the pumped region allows recovery of any helium that boils off. A small heater near the tip of the lance can be used to control the temperature from 4 K to approximately 300K depending upon the leak rate of helium from the helium reservoir into the sample space. The leak rate of helium is controlled (manually) via a needle valve. The control of the temperature by cooling from constantly evaporating helium and by joule heating by the heater can be used to control the rate of change of temperature and the final "set" temperature. Faster cooling can be achieved by opening the helium needle valve to a greater extent. A higher leak rate through the needle valve results in a higher pressure around the sample (e.g. 10-100 mbar) and greater cooling. Temperature is monitored every 1 second and measurements of electrical properties are started when change in temperature is less than 1 K in 1000 seconds.

Operation for measurement of Hall Resistance and mobility.

In order to measure the properties of the graphene and understand the band structure in more detail, the electrical properties of the graphene are measured as a function of temperature and magnetic field strength. In addition, the gate voltage of the graphene device is systematically varied to explore the Fermi level of the graphene.

As with other conductors, graphene is subject to Joule heating, so power levels (Voltage-current) need to be carefully controlled to avoid thermal damage to the graphene and changes of electrical properties due to local joule heating . A few millivolts and a current limit of 1-10 micro amps is a range that should not adversely affect the graphene sheet depending upon graphene mono layer integrity. To obtain a measure of such a system with low signal to noise resistance a lock in amplifier is used to control the current and measure the resistance in the circuit. A separate channel voltage source is used for the gate voltage.

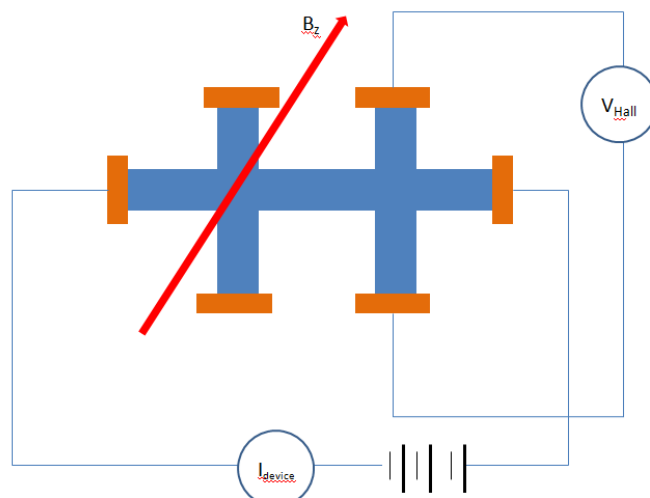


Figure 38. Set up for measurement of Hall voltage measurement (V_{Hall}) with magnetic field B_z perpendicular to the plane of the graphene with current I_{device} .

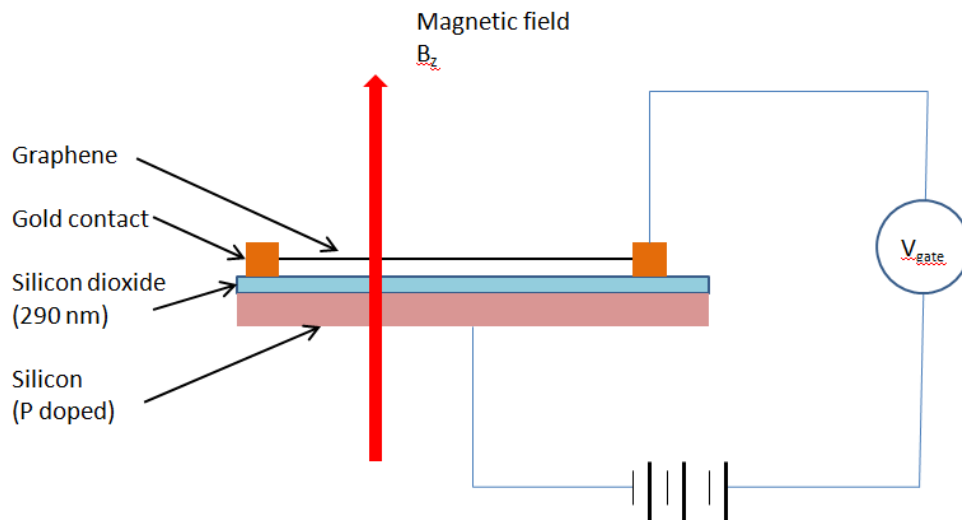


Figure 39. Hall measurement showing control of gate voltage (V_{gate}). Graphene shown resting on silicon dioxide layer. The magnetic field B_z is perpendicular to the plane of the graphene.

4.2 DEVICE MEASUREMENT ANALYSIS

Once a graphene fragment has been machined (lithography) and prepared; the measurement of I-V at set temperatures and magnetic field strength completed the data analysis can be undertaken. In this work much of the data was collected NOT by the author. However, the worked presented in this section has been completed by the author.

Several sets of data have been completed; two sets will be explored in detail.

1. Large data set. This data set scans the gate voltage from (+) 20 Volt to (+) 70 Volt in increments of 0.5 Volt and magnetic field strength from 0 to 14 Tesla in 0.05 Tesla increments. The total number of measurements being ca. 17 000 current readings.
2. A smaller focused data set of gate voltage scan from 40 to 50 Volts with increments of 0.2 Volts and magnetic field strength from 7.8 Tesla to 9.2 Tesla in increments of 0.01 Tesla with ca. 7 000 individual current measurements.

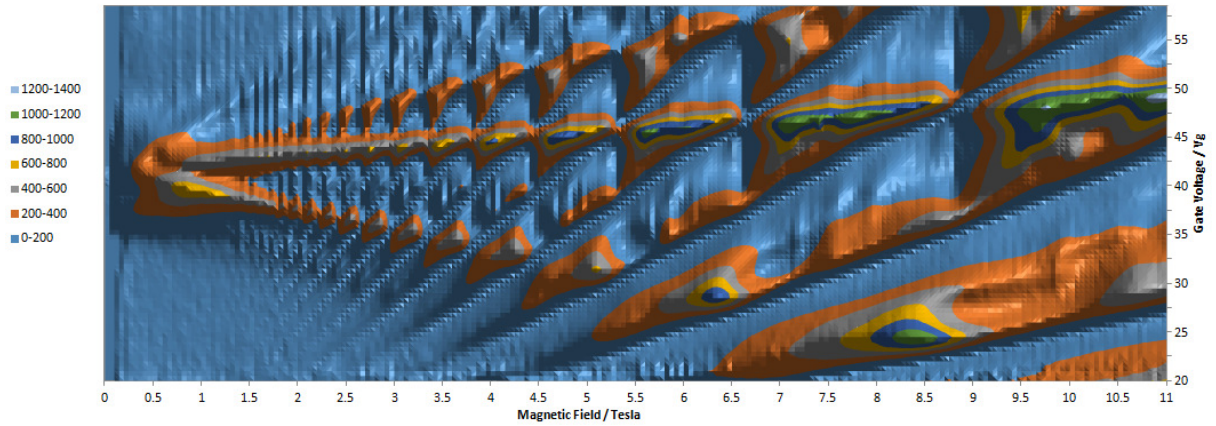
The current readings are themselves the "average" readings from the lock-in amplifier that have stabilised after a temperature or magnetic field change. In order to locate regions of high/low electron

mobility (low resistance vs. high resistance respectively) a calculation to find peaks and location/peaks or inflection is required.

Firstly, the gate voltage for un-biased conduction is found; as per theory this is at maximum resistance. This will be different for each sample. It was found for the sample that the gate voltage (maximum resistance) was at approximately (+) 43 Volts at zero magnetic field, indicating negative doping of the sample. This point can be labelled at $V_{g\ max}$ for convenience. $V_{g\ max}$ was found to vary depending on the magnetic field strength. For example, at 11 Tesla the $V_{g\ max}$ was approximately 49 volts.

Initially the data was sorted to ensure $V_{g\ max}$ was constant at each magnetic field setting, with $V_{g\ max}$ then set at $V_{gate} = 0$ volts. All other (gate voltage) readings were then referenced to the $V_{g\ max}$.

a.



b.

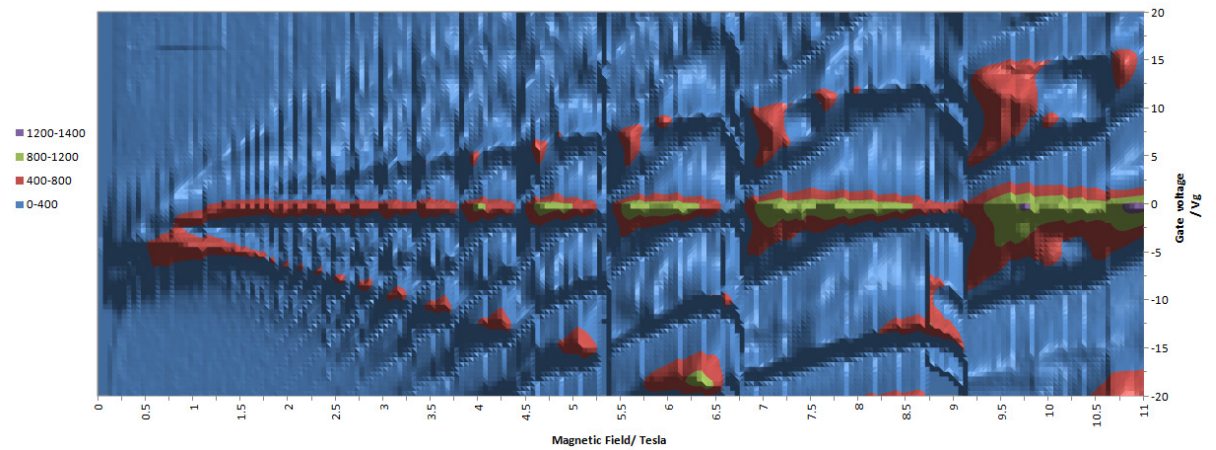


Figure 40. Plot of resistance (Ohm) on a surface graph of gate voltage (V_g) and magnetic field (B_z) showing difference between (a) data as collected (Gate voltage), and (b) Gate voltage set to zero volts at resistance (maximum). Notice the drifting to higher gate voltages as magnetic field strength increases in (a).

Whilst these low resolution graphs show key points, such as very high resistance peaks and high mobility "valleys" such as at 9, 7 and 5 Tesla. Figure 40 (b) illustrates this with variation of resistance plotted at corrected gate voltage to $V_g = 0$. The structure of the plot remain constant so this arbitrary correction may make the sample appear cleaner (and unbiased) but does not confound the analysis. All subsequent analysis is completed using the as-measured raw data.

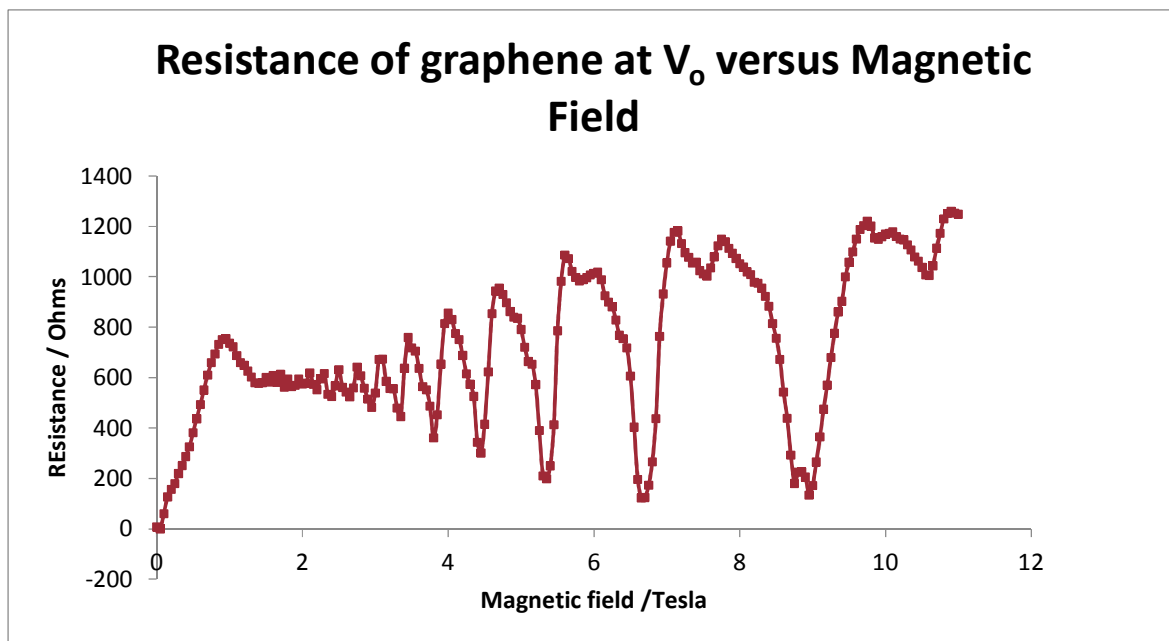


Figure 41. Plot of resistance at V_0 gate voltage as a function of magnetic field strength. Showing the development of ShD. Measurements taken at temperature 4K.

Whilst general "large" feature analysis provides some insights into the graphene system, it is important to fully analyse the data in the full breadth of magnetic field and range of gate voltages. For example the absolute values of resistance are dependent upon the graphene sample (size, shape, purity) and lithography (accuracy, metallisation). The patterns and values of energy changes are dependent upon the quantum system properties of graphene.

In this analysis accurate location of resistance maxima peaks in each dimension (gate voltage and magnetic field) will enable location of regions and quantum energy levels ("lines"). As the data points are equally spaced in gate-voltage (0.5 V) and magnetic field strength (0.05 T) location of resistance maxima can be achieved using the Savitzky–Golay¹ (de)convolution method. The Savitzky–Golay method is a simple application of the Newton method of approximation due to the constant, or digital, data points separation. As gate voltage determines the Fermi level measurement (or resistance maximum) it is convenient to use changes in resistance as a function of change in gate voltage as the primary data to analyse to find trends and locations of energy minima/maxima in the graphene device studied. Location of maxima in (rate of) change of gate voltage and magnetic field strength is straightforward; location of convolved peaks is best found using second (or third) derivative. Convolved, or hidden,

peaks can be observed by casual observation of data; accurate location of (hundreds of) peaks is best attempted using a simple algorithm. The simple script in the appendix indicates how data maxima are located and then sorted into nearest neighbours. Nearest neighbours that are connected, in graphene by discrete energy levels, can be plotted as slopes versus intercepts to identify families of energy levels. Such a diagram is presented in Figure 39, data from analysis of raw data(Figure 39) and analysed as per figure 36.

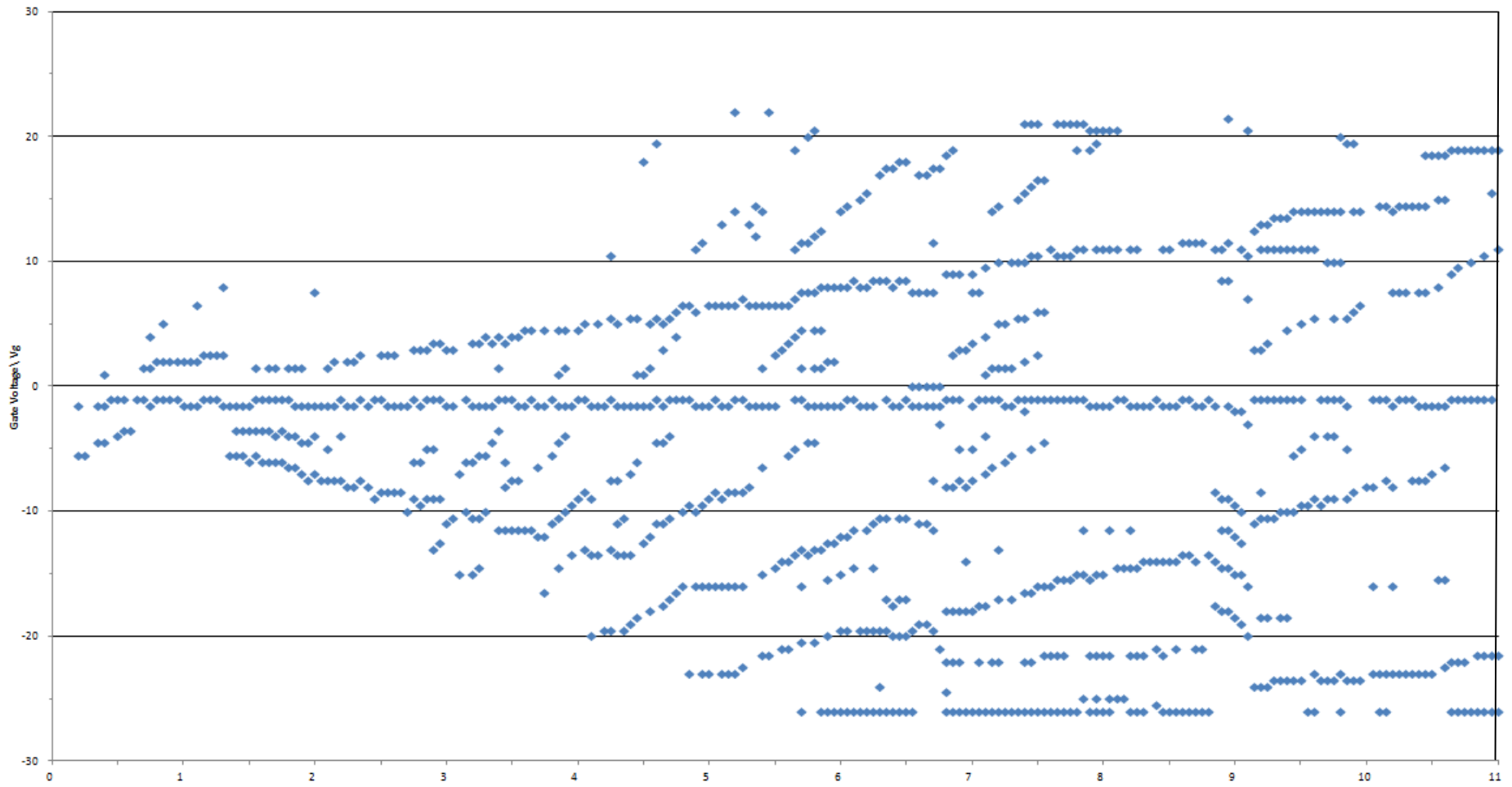


Figure 42. Analysis of raw data from Figure 40 to find resistance maximum. Each point shows the location of maximum in resistance. Measurements made with a lock in amplifier and taken at 4K.

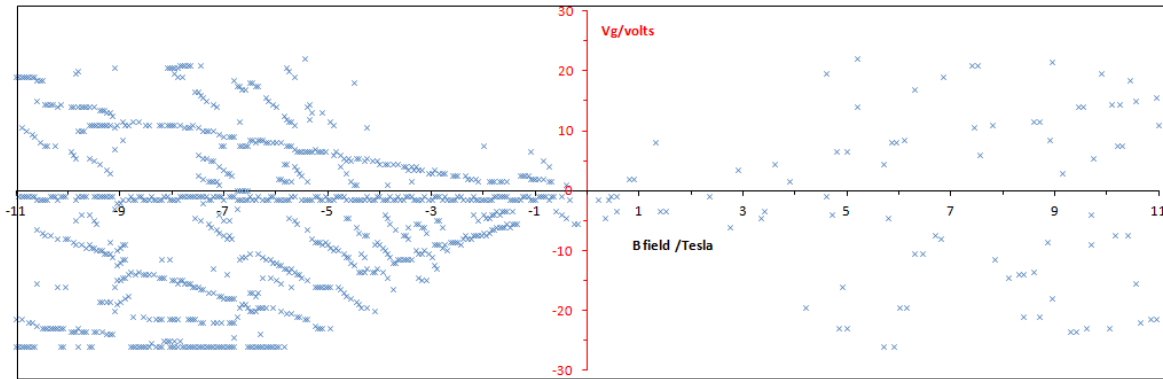


Figure 43. Plot of gradients of families of connected points from Figure 40. Points on the Left side shown R_{max} peaks that are linked together. Points on the Right side (positive) show R_{max} that are not part of a linked set of results.

4.3 REVIEW OF DATA ANALYSIS

The low magnetic field gives the normal Hall effect allowing the calculation of charge carriers.

$$R_{Hall} = \frac{B_z}{ned}$$

i.e

$$\frac{\partial R_{Hall}}{\partial B_z} = \frac{1}{ned}$$

With R_{Hall} (measured resistance) against B_z (measured magnetic field) and ned to be calculated as n number of charge carriers, e (charge on the electron) and d as the distance across the device. The normal, or classical, Hall effect occurs from $B_z = 0$ (Tesla) to $< B_z = 1.5$ (Tesla). In Figure 42 a plot of resistance indicates two regions: normal Hall effect and above 2 Tesla the quantum Hall effect. A plot of $\frac{n}{n_0}$ in Figure 42 allows a more accurate measurement, and calculation, of changes in magnetic field between each quantum state. The differences between $\frac{n}{n_0}$ as determined by magnetic field can be compared to the cyclotron energy at that point.

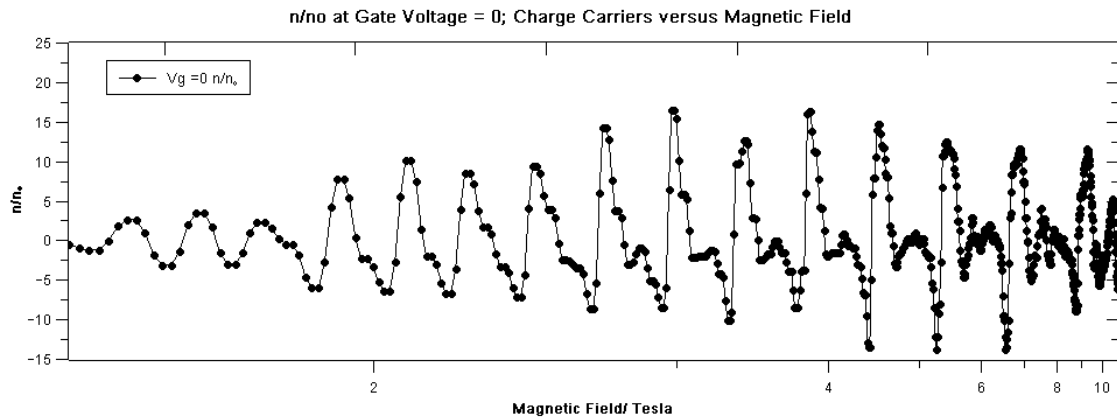


Figure 44. Plot of n/n_0 versus an inverse of magnetic field (B_z /Tesla). The added line is from Qti plot with cubic fitting (smoothed).

∂B_z /Tesla (frequency)	0.1	0.15	0.2	0.25	0.3	0.4	0.6
Maximum resistance Values/ Tesla	<i>0.825</i>	<i>1.025</i>	2.225	0.375	<i>0.075</i>	5.388	10.00
	<i>1.575</i>	<i>1.275</i>	2.975	2.425	4.138	6.288	
	4.04	1.425	3.175	3.575	4.488	6.888	
	4.84	1.775	3.375		5.038	8.55	
	4.938	1.925	3.838		7.60	9.25	
	5.84	2.075	7.9		8.95		
	6.09	2.675			9.65		
	6.188	2.825			10.60		
	7.29	5.938			10.95		
	7.388	6.738					
7.50	8.10						
	8.25						
	8.40						
Comment	<i>High frequency (near to sampling frequency of 0.05 Tesla)</i>		Well resolved peaks				

Table 3. Values of δB_z (Tesla) of maximum resistance (zero n/n_0) at Gate Voltage $V_g = 0$ from Figure 44. Values in *italics* are difficult to plot have a large error in measured value.

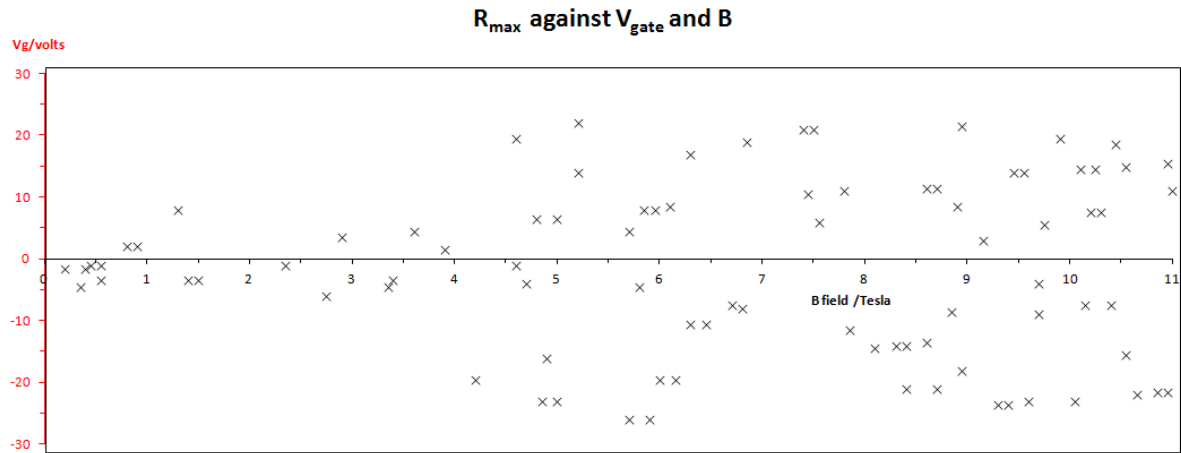


Figure 45. Viewing of points at R_{max} that are not associated with series of R_{max} in Figure 43.

4.4 CONCLUSION

The simple analysis of peaks using the Golay method (variation of Newton method) of interpolation/convolution allows analysis of data from I-V at various gate and magnetic field strengths. Accurate location of peaks in resistance (Fermi points) can be found both by looking at ∂V_{gate} and $\frac{n}{n_0}(\partial B_z)$ dimensions. The method is particularly suitable for finding secondary or convoluted (side) peaks in noisy or sparse data. Many of the data points of maximum resistance (Dirac point) are closely connected, or linked. Some points are not part of a (closely) connected series of lines (energy) and these are demonstrated in Figure 43.

4.5. NEXT STEPS

The data collected allows $\frac{n}{n_0}$ and an estimate of Γ/τ . The full analysis of a graphene-Hofstadter spectrum from a sample is hence possible. A simple test of the system would be to reverse the magnetic field in the solenoid. This would be a useful test of homogeneity of the magnetic field and sample homogeneity. The extra data could be used to reduce errors in measurement and observe the symmetry of positive and negative charge carriers at positive and negative gate voltages; fully symmetric behaviour should eliminate any variation due to sample preparation.

4.6 REFERENCES

1. Luo, J., Ying, K., He, P., Bai, J., (2005). Digital Signal Processing. 15 (2), pp. 122–136. "Properties of Savitzky–Golay digital differentiators"

APPENDIX A:

VBA CODE FOR SORTING CONNECTED RESISTANCE-MAXIMA (DIRAC POINTS)

```
Private Sub CommandButton1_Click()
```

```
Dim i As Integer
```

```
Dim r As Integer
```

```
Dim n As Integer
```

```
Dim dj As Integer
```

```
Dim kk As Integer
```

```
Dim k As Integer
```

```
Dim nearestb As Double
```

```
Dim nearestv As Double
```

```
Dim a As Double
```

```
Dim aa As Double
```

```
Dim b As Double
```

```
Dim bb As Double
```

```
Dim dB As Double
```

```
Dim dV As Double
```

set up variables

```
For i = 5 To 1300
```

```
If Range("N6").Offset(i, 0).Value < 0 Then
```

```
    i = i + 1
```

```
Else
```

```
    a = Range("N6").Offset(i, 0).Value
```

```
    aa = Range("N6").Offset(i, 1).Value
```

```
    n = 0
```

test if two points are close

```
Range("S6").Offset(i + i, 0).Value = a
Range("S6").Offset(i + i + 1, 0).Value = aa
```

End If

```
dB = 0
dV = 0
dj = 1
kk = 0
b = 0
bb = 0
n = 0
r = 0
nearestv = 7
```

set variables to start values

Do While dj > 0

Do While (i + kk + 1) < 1300

If Range("N6").Offset((i + kk + 1), 0).Value > 0 Then

b = Range("N6").Offset((i + kk + 1), 0)

bb = Range("N6").Offset((i + kk + 1), 1)

$dB = (b - a)^2$

$dV = (bb - aa)^2$

$nearestb = (dB + dV)^{(1 / 2)}$

If nearestb < nearestv Then

nearestv = nearestb

r = i + kk + 1

End If

measure nearest neighbours

If dV > 9 Then

kk = 1300

dV = 0

dB = 0

End If

End If

kk = kk + 1

Loop

if not nearest neighbour move on.

If nearestv < 0.25 Then

Range("S6").Offset(i + i, dj).Value = Range("N6").Offset(r, 0).Value

Range("S6").Offset(i + i + 1, dj).Value = Range("N6").Offset(r, 1).Value

n = n + 1

a = Range("N6").Offset(r, 0).Value

aa = Range("N6").Offset(r, 1).Value

kk = r - i

nearestv = 7

dj = dj + 1

nearest

Range("N6").Offset(r, -2).Value = i

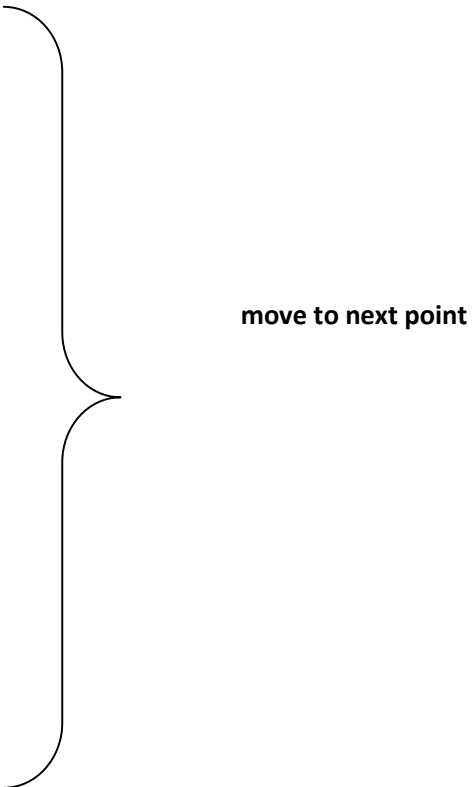
Range("N6").Offset(r, -3).Value = kk

Range("N6").Offset(r, 0).Value = -a

Range("N6").Offset(r, 1).Value = -aa

```
Else
Range("S6").Offset(i + i, -1).Value = n
Range("S6").Offset(i + i + 1, -1).Value = n
nearestv = 7
n = 0
dj = 0
kk = 0
r = 0
End If

Loop
Next i
End Sub
```



move to next point